

RESEARCH ARTICLE

10.1002/2015JA022216

Special Section:

Nature of Turbulence,
Dissipation, and Heating in
Space Plasmas: From Alfvén
Waves to Kinetic Alfvén Waves

Key Points:

- Mechanisms to produce kinetic Alfvén waves in pressure-balance structures
- Linear and nonlinear simulations of propagating Alfvén waves
- Kinetic effects due to the propagation of kinetic Alfvén waves

Correspondence to:

F. Pucci,
francesco.pucci@fis.unical.it

Citation:

Pucci, F., C. L. Vásconez, O. Pezzi, S. Servidio, F. Valentini, W. H. Matthaeus, and F. Malara (2016), From Alfvén waves to kinetic Alfvén waves in an inhomogeneous equilibrium structure, *J. Geophys. Res. Space Physics*, 121, 1024–1045, doi:10.1002/2015JA022216.

Received 30 NOV 2015

Accepted 4 FEB 2016

Accepted article online 6 FEB 2016

Published online 27 FEB 2016

From Alfvén waves to kinetic Alfvén waves in an inhomogeneous equilibrium structure

F. Pucci^{1,2}, C. L. Vásconez^{1,3}, O. Pezzi¹, S. Servidio¹, F. Valentini¹, W. H. Matthaeus⁴, and F. Malara¹

¹Dipartimento di Fisica, Università della Calabria, Cosenza, Italy, ²Now at Center for Mathematical Plasma Astrophysics, Departement Wiskunde, Universiteit Leuven, Leuven, Belgium, ³Observatorio Astronómico de Quito, Escuela Politécnica Nacional, Quito, Ecuador, ⁴Department of Physics and Astronomy, University of Delaware, Newark, Delaware, USA

Abstract Kinetic Alfvén waves are believed to primary form fluctuations in a hydromagnetic turbulence at scales of the order of the ion inertial length. We study a model where an initial Alfvén wave propagates inside an equilibrium structure which is inhomogeneous in the direction perpendicular to the equilibrium magnetic field. In a previous paper this situation has been considered in a particular configuration where the initial wave vector is parallel to the magnetic field and the wave is polarized perpendicular to the inhomogeneity direction. Here we consider other configurations, with a different polarization and possible initial oblique propagation. We employ numerical simulations, using both a Hall-magnetohydrodynamics and a Hybrid Vlasov-Maxwell model. Results show that in all the considered cases the time evolution leads to the formation of kinetic Alfvén waves within the inhomogeneity regions, which are identified by a comparison with analytical linear theory results. Then, in this context the formation of kinetic Alfvén waves seems to be a general phenomenon which could be also extended to more complex situations, like turbulence. Kinetic simulations show that kinetic Alfvén waves modify the ion distribution function, generating temperature anisotropy of both parallel and perpendicular to the local magnetic field as well as particle beams aligned along the local magnetic field. These results could be relevant both in the solar corona and in large-scale structures of the solar wind, where Alfvénic fluctuations are present along with large-scale inhomogeneities.

1. Introduction

In the inner heliosphere and in regions of high speed flow, solar wind turbulence at scales much larger than the proton inertial length is dominated by Alfvénic fluctuations, which are characterized by highly correlated velocity and magnetic field fluctuations and by low-level (with respect to the background values) density and magnetic field intensity variations [Belcher and Davis, 1971; Bruno and Carbone, 2005]. Several indications have been found of the presence of Alfvén waves also in the solar corona [Tomczyk et al., 2007; Tomczyk and McIntosh, 2009] from where the solar wind emanates.

In the scenario of solar wind turbulence, the role of spectral anisotropy must be taken into account. Theoretical studies, indeed, have shown that in a magnetohydrodynamics (MHD) turbulence the energy cascade preferentially takes place perpendicularly to the background magnetic field \mathbf{B}_0 [e.g., Shebalin et al., 1983; Carbone and Veltri, 1990; Oughton et al., 1994]. Then, it is expected that at smaller scales the fluctuation energy tends to concentrate in nearly perpendicular wave vectors. In fact, observations show that the distribution of wave vectors of magnetic fluctuations has a significant population quasi-perpendicular to the mean magnetic field [Matthaeus et al., 1986, 1990]. Moreover, all the above features, such as Alfvénic correlations and spectral anisotropy, as well as the presence of several characteristic length scales, can interact with large-scale structures such as shears and magnetic equilibria, with a subsequent generation of wave-like activity. The description of the full picture is a complex task, which could be addressed by means of simplified models.

Waves belonging to the Alfvén branch, with wavelengths comparable with the proton inertial length d_p and wave vectors nearly perpendicular to the mean magnetic field are often indicated as “kinetic Alfvén waves” (KAWs). During the last decades, KAWs have received considerable attention and have been studied in detail due to their possible role in a normal mode description of the turbulent cascade. Since the MHD cascade favors nearly perpendicular wave vectors, the expectation within a wave perspective would be that

fluctuations having a character resembling KAWs are naturally present at scales of the order of d_p . An extensive analysis of the KAW physics is found in *Hollweg* [1999] (see also references therein for a more complete view on the subject). Many solar wind observational analyses [*Bale et al.*, 2005; *Sahraoui et al.*, 2009; *Podesta and TenBarge*, 2012; *Salem et al.*, 2012; *Chen et al.*, 2013; *Kiyani et al.*, 2013], theoretical works [*Howes et al.*, 2008a; *Schekochihin et al.*, 2009; *Sahraoui et al.*, 2012] as well as numerical simulations [*Gary and Nishimura*, 2004; *Howes et al.*, 2008b; *TenBarge and Howes*, 2012] have suggested that fluctuations near the end of the magnetohydrodynamics inertial cascade range may consist primarily of KAWs and that such fluctuations can play an important role in the dissipation of turbulent energy. Due to a nonvanishing electric field parallel component associated with KAWs, these waves have also been considered in the problem of particle acceleration [*Voitenko and Goossens*, 2004; *Décamp and Malara*, 2006]. One should also recall that the interaction of oppositely propagating Alfvén waves always produces a parallel electric field. Recently, *Vasconez et al.* [2014] have studied collisionless Landau damping and wave-particle resonant interactions in KAWs.

There are also situations simpler than fully developed turbulence where formation of small scales in the direction perpendicular to a background magnetic field could take place. For instance, this effect appears in the context of nonlinear MHD when imposed parallel-propagating waves interact with an inhomogeneous background consisting either of pressure-balanced structures or velocity shears [*Ghosh et al.*, 1998]. In 2-D inhomogeneous equilibria, where quantities vary in the direction transverse to the magnetic field, small amplitude waves can be subject to phase mixing [*Heyvaerts and Priest*, 1983], in which differences in group velocity at different locations progressively bend wavefronts, thus generating small scales in the perpendicular direction. Another mechanism is resonant absorption which concentrates the wave energy in a narrow layer where the wave frequency locally matches a characteristic frequency. These processes have been studied both by a normal modes approach [*Kappraft and Tataronis*, 1977; *Mok and Einaudi*, 1985; *Steinolfson*, 1985; *Davila*, 1987; *Hollweg*, 1987; *Califano et al.*, 1990, 1992] and by considering the evolution of an initial disturbance [*Lee and Roberts*, 1986; *Malara et al.*, 1992, 1996]. Effects of density stratification and magnetic line divergence [*Ruderman et al.*, 1998], as well as nonlinear coupling with compressive modes [*Nakariakov et al.*, 1997, 1998], and evolution of localized pulses [*Kaghashvili*, 1999; *Tsiklauri and Nakariakov*, 2002; *Tsiklauri et al.*, 2003] have also been considered. The propagation of MHD waves in inhomogeneous magnetic fields containing null points has also been studied in detail [*Landi et al.*, 2005; *McLaughlin et al.*, 2011; *Pucci et al.*, 2014], finding a fast formation of small scales perpendicular to the ambient magnetic field. In 3-D inhomogeneous equilibria this process has been considered in the small wavelength limit [*Similon and Sudan*, 1989; *Petkaki et al.*, 1998; *Malara et al.*, 2000], also within the problem of coronal heating [*Malara et al.*, 2003, 2005, 2007]. Particle acceleration in phase mixing of Alfvén waves in a dispersive regime has been studied both in 2-D [*Tsiklauri et al.*, 2005; *Tsiklauri*, 2011] and in 3-D [*Tsiklauri*, 2012] configurations. Finally, instabilities generating KAWs in plasma with transverse density modulations have been considered by *Wu and Chen* [2013]. Similar ideas involving dissipative mechanisms related to interaction of Alfvén waves or KAWs and phase mixing have been examined in the context of the magnetospheric plasma sheet [*Lysak and Song*, 2011] and in coronal loops [*Ofman and Aschwanden*, 2002]. It has been shown that ion-scale shear Alfvén waves can be excited by ion beams in the solar wind [*Hellinger and Trávníček*, 2011, 2013], and these can contribute to the formation of KAWs [*Nariyuki et al.*, 2014a]. Many observations have shown that the proton distribution function in the solar wind can include a beam directed in the direction parallel to the local magnetic field [*Marsch*, 2006; *Marsch et al.*, 1982; *Goodrich and Lazarus*, 1976], with a drift speed of the order of the local Alfvén velocity [*Goldstein et al.*, 2000; *Tu et al.*, 2004]. Physical processes which can lead to the formation of this beam have also been considered [*Araneda et al.*, 2008; *Valentini et al.*, 2008; *Matteini et al.*, 2010; *Valentini et al.*, 2011a, 2011b; *Nariyuki et al.*, 2014b]. The above considerations suggest that the interaction of Alfvén waves with inhomogeneous background structures might represent a mechanism to produce KAWs [*Hollweg*, 1999], when the wavelength of waves becomes small enough to be comparable with the proton inertial length d_p . This effect could work, for instance, in the solar corona where the background magnetic field is clearly nonuniform and where the presence of Alfvén waves has been ascertained, or in the solar wind where large-scale inhomogeneities like current sheets and velocity shears are present. In a recent paper *Vasconez et al.* [2015] (hereafter, Paper I) have studied a problem in which phase mixing acting on an initial Alfvén wave generates KAWs localized in regions where the background is inhomogeneous. In that study, both fluid and kinetic simulations have been employed; in particular, it has been found that the KAWs produced by this mechanism can modify the proton velocity distribution function (VDF), generating temperature anisotropy and beams of particles moving parallel to the magnetic field. In the configuration considered in Paper I the initial perturbation is

propagating parallel to the background magnetic field $\mathbf{B}^{(0)}$ and it is linearly polarized along a direction which is perpendicular both to $\mathbf{B}^{(0)}$ and to the inhomogeneity direction. As a consequence, the polarization remains transverse to the wave vector up to the time in which dispersive effects become active. This gives a smooth evolution of the initial Alfvén wave toward a KAW.

Clearly, the situation considered in Paper I is a particular case, and there are other possible configurations in which an initial Alfvén wave propagates in a transverse inhomogeneous structure. The aim of the present paper is to generalize the results of Paper I by extending the study to such different configurations, thus investigating the possibility to generate KAWs in more general physical situations. In particular, we want to clarify the role of phase mixing in the generation of KAWs, by considering situations where phase mixing may be active or not. Both fluid (Hall-MHD) and kinetic (Hybrid Vlasov-Maxwell) simulations will be employed in the present study, considering both small- and large-amplitude cases to investigate possible effects of nonlinearities.

In section 2 the two models (fluid and kinetic) are presented; the results of simulations are described in section 3, while a discussion and a summary of results are given in section 4. Finally, in Appendix A linear normal modes are described within the Hall-MHD framework.

2. Hall-MHD and Hybrid Vlasov-Maxwell Numerical Simulations

We study the evolution of Alfvén waves propagating in an inhomogeneous equilibrium pressure-balanced structure by means of 2.5-D numerical simulations. Perturbations wavelength is large enough to make dispersive effects initially negligible. During the time evolution, the interaction between the perturbation and the equilibrium inhomogeneity generates small scales structures in which both dispersive and kinetic effects play an important role. We first study the linear case, where the perturbation amplitude is small compared with the equilibrium quantities, using a Hall-MHD (HMHD) numerical code. Then we move to the nonlinear case in which we use a hybrid Vlasov-Maxwell (HVM) code in order to single out the role of kinetic effects in the evolution of the proton distribution function. In this section we present the two models and describe the simulation initial conditions.

The HMHD description of a plasma composed by protons and electrons is valid under the following assumptions: the plasma is quasi-neutral ($n_p \simeq n_e$, with n_e and n_p the number densities of protons and electrons, respectively), the temperature of the two species are the same $T_p = T_e = T_0$, the scale considered is sufficiently large to neglect the electron mass ($m_e \ll m_p$) and the characteristic plasma speed is small compared to the speed of light, so that the displacement current term in the Ampere equation can be neglected. Under these assumptions the plasma can be described by the HMHD equations, here written in nondimensional form:

$$\frac{\partial \rho}{\partial t} + \nabla \cdot (\rho \mathbf{v}) = 0 \quad (1)$$

$$\frac{\partial \mathbf{v}}{\partial t} + (\mathbf{v} \cdot \nabla) \mathbf{v} = -\frac{\tilde{\beta}}{2\rho} \nabla(\rho T) + \frac{1}{\rho} [(\nabla \times \mathbf{B}) \times \mathbf{B}] \quad (2)$$

$$\frac{\partial \mathbf{B}}{\partial t} = \nabla \times \left[\mathbf{v} \times \mathbf{B} - \frac{\tilde{\epsilon}}{\rho} (\nabla \times \mathbf{B}) \times \mathbf{B} \right] \quad (3)$$

$$\frac{\partial T}{\partial t} + (\mathbf{v} \cdot \nabla) T + (\gamma - 1) T (\nabla \cdot \mathbf{v}) = 0 \quad (4)$$

In equations (1)–(4) the mass density ρ (which is only due to protons) is normalized to a typical density $\tilde{\rho}$, temperature T to a typical value \tilde{T} , the pressure $p = \rho T$ due to both protons and electrons is normalized to the value $\tilde{p} = 2\kappa_B \tilde{\rho} \tilde{T} / m_p$, κ_B being the Boltzmann constant and m_p the proton mass. The spatial coordinates $\mathbf{x} = (x, y)$ are normalized to a typical length \tilde{L} , magnetic field \mathbf{B} is normalized to a typical magnetic field \tilde{B} , fluid velocity \mathbf{v} to the typical Alfvén speed $\tilde{c}_A = \tilde{B} / (4\pi \tilde{\rho})^{1/2}$, time t to the Alfvén time $\tilde{t}_A = \tilde{L} / \tilde{c}_A$. Moreover, $\tilde{\beta} = \tilde{p} / (\tilde{B}^2 / 8\pi)$ is a typical value for the kinetic to magnetic pressure ratio; $\gamma = 5/3$ is the adiabatic index; $\tilde{\epsilon} = \tilde{d}_p / \tilde{L} = 0.125$ is the Hall parameter measuring the relative amplitude of the Hall term with respect to the $\mathbf{v} \times \mathbf{B}$ term in the Ohm's law, $\tilde{d}_p = \tilde{c}_A / \tilde{\Omega}_{cp} = \tilde{c}_A m_p c / (q \tilde{B})$ being the proton inertial length.

It is worth to note that equations (1)–(4) are ideal and adiabatic; however, to ensure numerical stability, we included a hyperviscosity and a hyperresistivity term in equations (2)–(4). Details about the numerical algorithm can be found in Paper I.

The nonlinear simulations have been performed by using an HVM code [Valentini *et al.*, 2007] in which the Vlasov equation for protons is solved in a 2D-3V (two dimensional in physical space and three dimensional in velocity space) phase space, while electrons are an ideal and isothermal fluid, whose temperature is equal to the initial proton temperature. Equations solved by the HVM code in nondimensional units are the following:

$$\frac{\partial f}{\partial t} + \mathbf{u} \cdot \nabla f + \frac{1}{\tilde{\epsilon}} (\mathbf{E} + \mathbf{u} \times \mathbf{B}) \cdot \frac{\partial f}{\partial \mathbf{u}} = 0 \quad (5)$$

$$\mathbf{E} = -\mathbf{v} \times \mathbf{B} + \frac{\tilde{\epsilon}}{n} \left(\mathbf{j} \times \mathbf{B} - \frac{\tilde{\beta}}{2} \nabla P_e \right) \quad (6)$$

$$\frac{\partial \mathbf{B}}{\partial t} = -\nabla \times \mathbf{E} \quad ; \quad \nabla \times \mathbf{B} = \mathbf{j} \quad (7)$$

where $f = f(\mathbf{x}, \mathbf{u}, t)$ is the proton distribution function, $n = \int d^3u f$ is the proton number density normalized to $\tilde{n} = \tilde{\rho}/m_p$, \mathbf{B} is the magnetic field normalized to \tilde{B} , $\mathbf{v} = n^{-1} \int d^3u f \mathbf{u}$ is the proton bulk velocity normalized to \tilde{c}_a , \mathbf{E} is the electric field normalized to $\tilde{E} = (\tilde{c}_a \tilde{B})/c$ (where c is the speed of light), the spatial coordinates are normalized to \tilde{L} , time is normalized to $\tilde{t}_a = \tilde{L}/\tilde{c}_a$, \mathbf{j} is the current density normalized to $\tilde{j} = c\tilde{B}/(4\pi\tilde{d}_p)$, and P_e is the electron pressure normalized to \tilde{p} . These equations are obtained under the assumption of quasi-neutrality and in the low-frequency regime where the displacement current in Ampere equation can be neglected. The value of the electron pressure is set equal to the initial value of the proton pressure, and their inertia effects are neglected. The numerical grid is discretized with 256×1024 points in the physical domain and 51^3 points in the velocity domain. Numerical stability is ensured by Landau damping and by dissipation inherent in the finite difference methods employed in the HVM algorithm. Periodicity is imposed in the physical space, while in the velocity domain the distribution function f is set equal to zero for $|u_i| > u_{\max}$ ($i = x, y, z$), where $u_{\max} = 5v_{\text{th},p}$, $v_{\text{th},p}$ being the proton thermal speed. A detailed description of the numerical method employed to solve equations (5)–(7) can be found in Valentini *et al.* [2007]. We remark that low-noise Vlasov simulations allow to recover details about the VDFs dynamics [Servidio *et al.*, 2012; Greco *et al.*, 2012; Perrone *et al.*, 2014; Valentini *et al.*, 2014; Servidio *et al.*, 2015].

For both models we choose a spatial domain $D(x, y) = [0, 2\pi] \times [0, 2\pi]$ and we set the same initial condition, which consists in a pressure-balanced equilibrium structure with a perturbation superposed on it. The equilibrium magnetic field, that varies only in the y direction, has this form:

$$\mathbf{B}^{(0)} = B^{(0)}(y) \cos(\theta) \mathbf{e}_x + B^{(0)}(y) \sin(\theta) \mathbf{e}_z, \quad (8)$$

where

$$B^{(0)}(y) = 1 + \frac{b_m - 1}{1 + \left(\frac{y - \pi}{2\pi h}\right)^r}, + \alpha \left(\frac{y}{\pi} - 1\right)^2 \quad (9)$$

\mathbf{e}_x and \mathbf{e}_z being the x and z unit vectors, θ the angle that $\mathbf{B}^{(0)}$ forms with \mathbf{e}_x , $b_m = 1.5$, $h = 0.2$, $r = 10$, and

$$\alpha = \frac{(b_m - 1)r}{2(2h)^r \left[1 + \left(\frac{1}{2h}\right)^r\right]^2} \simeq 2.62 \times 10^{-4}. \quad (10)$$

The value of α has been set in order to make the first derivatives of $B^{(0)}(y)$ null at the two boundaries $y = 0$ and $y = 2\pi$. The field $B^{(0)}(y)$ is symmetrical with respect to $y = \pi$, that is, the middle of the domain, where it reaches the maximum value b_m . It is worth to note that the $B^{(0)}(y)$ intensity is almost homogeneous in the central part of the domain, while moving to the sides it rapidly decreases to a smaller value. The two shear regions where $B^{(0)}(y)$ sharply varies can be seen in Figure 1 and have a width $\Delta y_s \sim 1$. In these regions two strong current sheets in the z direction are present. The proton temperature is homogeneous, its value being $T^{(0)} = 1$, and

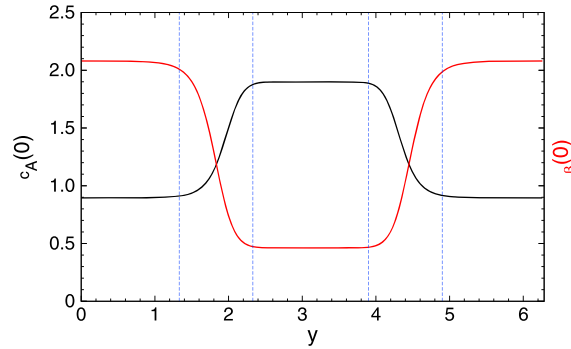


Figure 1. Alfvén velocity $c_A^{(0)}$ (black solid line) and plasma $\beta^{(0)}$ (red solid line) in the equilibrium structure as a function of y . The dashed blue lines delimit the two shear regions.

the velocity is null at the initial time. The mass density $\rho^{(0)}$ is set to guarantee equilibrium between kinetic and magnetic pressure:

$$\frac{\tilde{\beta}}{2} \rho^{(0)}(y) T^{(0)} + \frac{B^{(0)2}(y)}{2} = P_T^{(0)} \quad (11)$$

where $P_T^{(0)} = 1.748$ and $\tilde{\beta} = 2$. The initial Alfvén velocity $c_A^{(0)} = B^{(0)}(y) / \sqrt{\rho^{(0)}(y)}$ and plasma $\beta^{(0)}(y) = (c_s^{(0)} / c_A^{(0)})^2$ profiles (where $c_s^{(0)} = (\gamma T^{(0)})^{1/2}$ is the sound speed) are plotted in Figure 1 as functions of y . The Alfvén velocity is larger in the middle of the domain and decreases in the shear regions to reach a lower value on the two sides. On the other hand, the plasma β has an opposite trend: it varies from smaller values $\beta < 1$ in the middle of the domain to higher values $\beta > 1$ in the two side regions. In Paper I authors considered this equilibrium structure in the particular case where $\theta = 0$. This case corresponds to an in-plane equilibrium magnetic field.

The initial perturbation represents a linearly polarized Alfvén wave. Thus, the polarization direction must be perpendicular both to $\mathbf{B}^{(0)}$ and to the initial wave vector \mathbf{k}_0 . In the initial condition \mathbf{k}_0 is oriented along x , while $\mathbf{B}^{(0)}$ is in the xz plane. Thus, the initial perturbation must be polarized along y , at least for $\theta \neq 0$. Then, we choose the following form for the initial velocity and magnetic field perturbation:

$$\mathbf{B}^{(1)}(x, y, t = 0) = a \cos(x) \mathbf{e}_y, \quad \mathbf{v}^{(1)}(x, y, t = 0) = -a [\rho^{(0)}(y)]^{-1/2} \cos(x) \mathbf{e}_y \quad (12)$$

where a gives the perturbation amplitude and $k_0 = 1$.

Equation (12) represents an Alfvén wave in the MHD limit, which holds when $k_0 d_p \ll 1$. In our simulations, since density is not homogeneous, the proton inertial length varies in the domain so that $0.11 \leq k_0 d_p \leq 0.16$. Then, this initial condition is approximately in the MHD regime: for instance, the phase velocity of parallel-propagating Alfvén waves is of the order of 90% of the Alfvén velocity. In the case $\theta = 0$ (in-plane magnetic field), $\mathbf{B}^{(0)}$ and \mathbf{k}_0 are parallel and directed along x , so the initial polarization could be directed along any direction in the yz plane. In practice, for $\theta = 0$ it is sufficient to consider only two independent orientations for the initial polarization: the first one is along y and has again the form (12); the second one is along z and has the form (12) in which the unit vector \mathbf{e}_y is replaced by the unit vector \mathbf{e}_z . The latter case corresponds to the configuration studied in Paper I. Then, in the present paper we will consider the other two possibilities, using the form (12) for the velocity and magnetic field perturbation and considering both the case $\theta = 0$ and a case with $\theta \neq 0$, for which we set $\theta = \pi/4$. In both cases, the initial density and temperature fluctuations are vanishing: $\rho^{(1)}(x, y, t = 0) = 0$, $T^{(1)}(x, y, t = 0) = 0$.

Numerical parameters of the various simulations performed are summarized in Table 1. Note that the wave amplitude chosen for the HMHD runs is $a = 0.01$, while we set $a = 0.25$ for the HVM simulations in order to make the effects on the particle distribution function more visible. We will refer to the HMHD simulation with $\theta = 0$ and $\theta = \pi/4$ as RUN 1 and RUN 2, respectively, and to the corresponding HVM simulation as RUN 3 and RUN 4, respectively.

Table 1. Numerical Parameters in Simulations

RUN	Type	Spatial Resolution ($n_x \times n_y$)	Amplitude (a)	Hall Parameter ($\tilde{\epsilon}$)	θ
1	HMHD	256×256	0.01	0.125	0
2	HMHD	256×256	0.01	0.125	$\pi/4$
3	HVM	256×1024	0.25	0.125	0
4	HVM	256×1024	0.25	0.125	$\pi/4$

3. Numerical Results

We first summarize results obtained in Paper I in order to make a comparison with the new configurations considered here. In Paper I the initial Alfvénic perturbation, which propagates in the inhomogeneous equilibrium structure, undergoes phase mixing, as predicted by the linear MHD theory [Heyvaerts and Priest, 1983]. Phase mixing is localized in the two shear layers, where the Alfvén velocity is inhomogeneous. The wave vector of the initial perturbation is $k_0 = k_{\parallel} = 1 \ll \tilde{\epsilon}^{-1}$, so that dispersive effects are initially negligible. However, in consequence of phase mixing, within the shear layers the perpendicular wave vector k_{\perp} of the perturbation increases in time, while the parallel wave vector k_{\parallel} remains constant. When the condition $k_{\perp} \sim d_p^{-1} \gg k_{\parallel}$ is satisfied, the Alfvén wave becomes a kinetic Alfvén wave (KAW), in which dispersive effects are no longer negligible. In particular, the initial linear polarization is transformed into an elliptical polarization. KAWs formed by this mechanisms are initially localized within the shear layers; however, due to a nonvanishing perpendicular group velocity $v_{g\perp}$, KAWs drift laterally and move into the homogeneous regions. This time evolution is observed in the low-amplitude case, and a similar behavior is found also in the nonlinear case, both in HMHD and in HVM simulations. Kinetic simulations show that the proton VDF locally departs from the Maxwellian shape in the regions where KAWs are present, and it remains essentially gyrotropic with respect to the local magnetic field direction. Moreover, the parallel temperature T_{\parallel} can locally become either larger or smaller than the perpendicular temperature T_{\perp} , according to the phase of the KAW. In regions where T_{\parallel} is particularly large, a distinct protons beam moving parallel to the local magnetic field is recovered. The beam velocity is comparable with the KAW parallel velocity of propagation, indicating that KAWs can accelerate protons along the magnetic field, at least for a large-amplitude initial perturbation. KAWs are also characterized by a parallel electric field E_{\parallel} , due to electron pressure gradients. The related electric potential energy modulation is of the order of the proton thermal energy; thus indicating that the observed particle beams are probably generated by E_{\parallel} associated with KAW.

3.1. HMHD Simulation in the In-Plane $B^{(0)}$ Case

We discuss now the results relative to RUN 1. In this case both the initial perturbation and the equilibrium magnetic field are in the plane xy . Here the phenomenology is more complex and richer than that observed in Paper I, though KAWs formation is found also in this case. Since the equilibrium structure quantities depend only on y , we define quantities relative to the perturbation at any time as $\delta g = g - \langle g \rangle_x$, where g indicates any physical quantity and $\langle g \rangle_x$ is its average in the x direction. At the beginning of the simulation a rapid formation of compressive fluctuations is observed in the two shear layers. In particular, density perturbations are generated. This phenomenon, which was absent in Paper I, is due both to the perturbation y polarization and to the background density inhomogeneity; in fact, from the continuity equation at the initial time we derive

$$\left. \frac{\partial \rho}{\partial t} \right|_{t=0} = -\frac{\partial (\rho^{(1)})}{\partial y} = -\frac{a \cos(x)}{2\sqrt{\rho^{(0)}(y)}} \frac{d\rho^{(0)}}{dy} \quad (13)$$

where we used equation (12). Equation (13) indicates that density fluctuations are initially generated at positions where $\rho^{(0)}$ is inhomogeneous, with the same periodicity in the x direction as the initial wave and a width in the y direction of the order of the shear layer width $2\pi h \sim 1$.

At subsequent times this perturbation remains partially confined within the shear layers. This density perturbation has a nonvanishing time average $\langle \delta \rho \rangle_t$, where the average is calculated over the whole simulation time. $\langle \delta \rho \rangle_t$ represents a static component of the density perturbation and it is plotted in Figure 2, along with the time-averaged temperature fluctuation $\langle \delta T \rangle_t$. It can be seen that the static components of density and

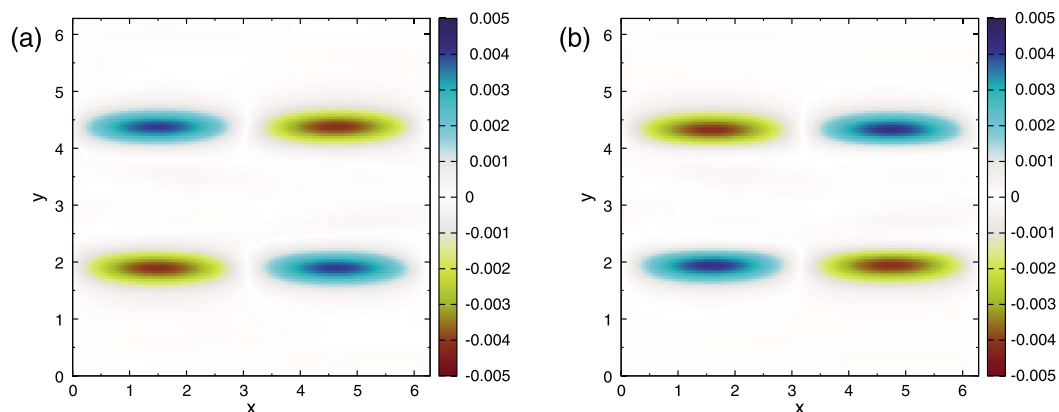


Figure 2. Entropy waves in shear regions: (a) Time-averaged density fluctuation $\langle \delta \rho \rangle_t$ and (b) temperature fluctuation $\langle \delta T \rangle_t$ (RUN 1).

temperature fluctuations are perfectly anticorrelated; then we can interpret such fluctuations as entropy waves, which are static pressure-balanced structures in which neither velocity nor magnetic field fluctuations are involved. The amplitude of the entropy waves is $\sim 5 \times 10^{-3}$, which is $\sim 25\%$ of the amplitude of the density perturbation in the shear layers. The remaining part corresponds to a density perturbation which propagates along x remaining essentially confined within the shear layers. This perturbation could tentatively be attributed to a slow-mode wave, whose group velocity is directed along $B^{(0)}$ in the MHD limit.

Another phenomenon that develops starting from the initial time is the formation of fast-mode perturbations which have origin at the shear layers and propagate perpendicularly to the background magnetic field. In Figure 3 the rapid formation and propagation of this structure is shown. We can see that at time $t = 2$ this kind of waves are exiting the domain and, because of periodicity, they enter from the other side. This propagation of a fast-mode perturbation goes on along all the simulations and involves only vector components in the xy plane.

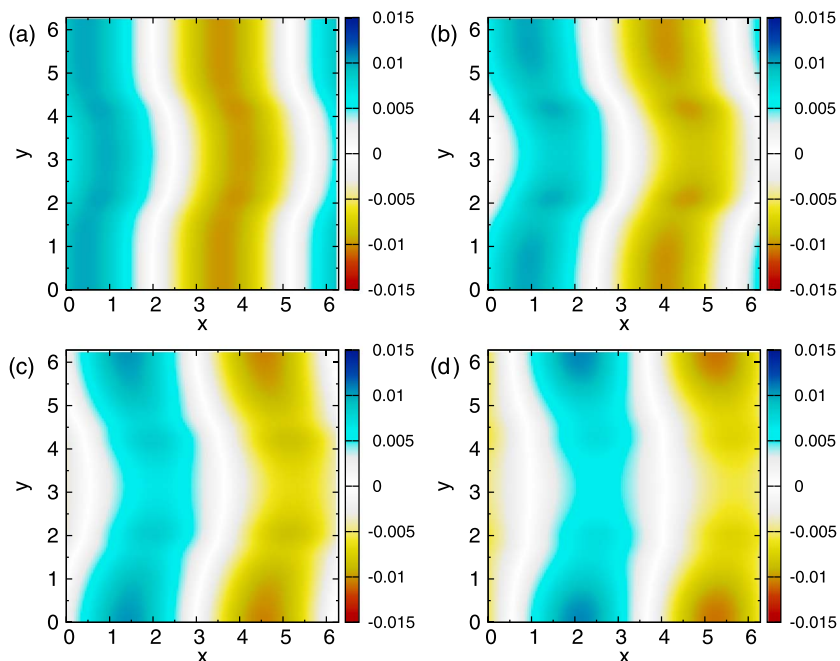


Figure 3. Fast wave generation at initial times (RUN 1). $\delta B_y(x, y)$ is plotted at the time (a) $t = 0.5$, (b) $t = 1.0$, (c) $t = 1.5$, (d) $t = 2.0$.

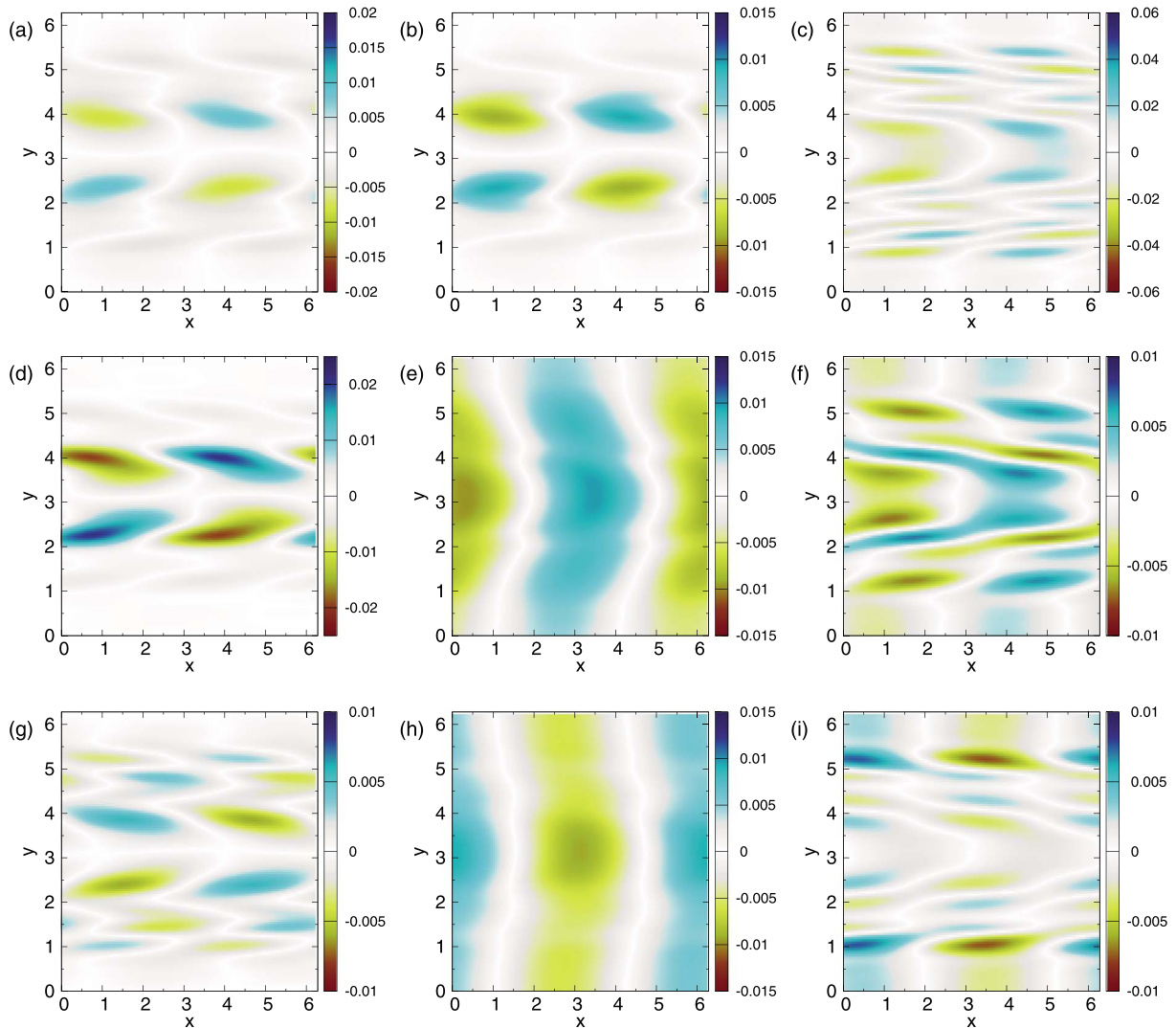


Figure 4. Contour plots of (a) $\delta\rho$, (b) δT , (c) δj_z , (d) δv_x , (e) δv_y , (f) δv_z , (g) δB_x , (h) δB_y , and (i) δB_z at time $t = 15.0$ (RUN 1).

Hence, in the first stage of the time evolution the initial perturbation couples with the background inhomogeneity producing compressive perturbations belonging to the three compressive MHD modes (fast, slow, and entropy waves). We note that a similar behavior was also found in previous purely MHD simulations [Malara *et al.*, 1996]. These features were not found in the linear simulations in Paper I, except for much smaller compressive fluctuations generated by higher-order nonlinear couplings.

As time goes on, other dynamical features can be appreciated. Figure 4 shows the contour plots of several quantities at time $t = 15$ for RUN 1. A relevant characteristic is the lack of phase mixing of the initial wave, as it can be seen in the plots of δv_y and δB_y (see Figures 4e and 4h). This is an important difference with respect to the Paper I configuration, where phase mixing was present and produced small scales, and it is in accordance with purely MHD simulations [Malara *et al.*, 1996]. We remark that phase mixing appears as a wavefront stretching due to differences in phase speeds.

In Figure 4 the formation of fluctuations in the z direction can be observed (see Figures 4f and 4i). Since in the MHD limit an initial 2-D configuration must necessarily remain 2-D for subsequent times, this phenomenon can only be due to dispersive effects that are more relevant at smaller scales. These fluctuations are localized in the shear layers and exhibit a small transverse size (about the shear layer width $\Delta y_s \sim 1$), which is larger than the one observed in Paper I. These structures are still visible at subsequent times (not shown here), outside the shear layers where they have drifted in the meanwhile.

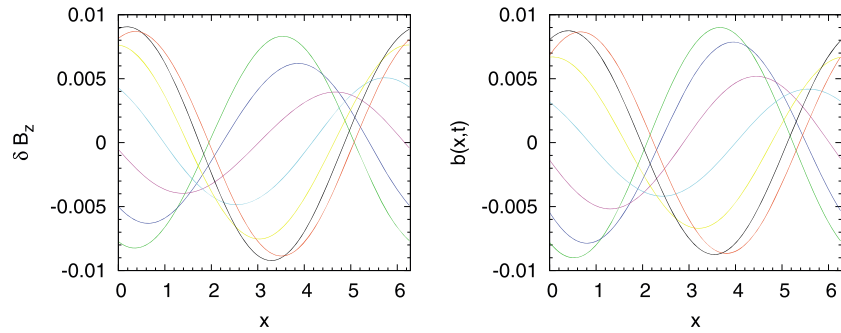


Figure 5. (left) $\delta B_z(x, y=5, t)$ and (right) $b(x, t)$ as functions of x at different times: $t=11.0$ (green), $t=11.5$ (blue), $t=12.0$ (purple), $t=12.5$ (light blue), $t=13.0$ (yellow), $t=13.5$ (black), and $t=14.0$ (orange).

However, since no phase mixing is present, another kind of coupling between the initial wave and the background inhomogeneity must be responsible for such a small-scale structure formation. We will show that these structures can be identified as the z components of KAW fluctuations.

To study in more detail the nature of these perturbations we plotted the profile of δB_z as a function of x at $y=5$ for different times (Figure 5, left). These profiles are sinusoidal with a wavelength equal to the domain size (2π), propagating in the direction of increasing x ; their amplitude is not constant in time, but it is modulated, changing periodically between a maximum and a minimum value. We can interpret this behavior as due to the superposition of two waves with different amplitudes; these two waves have the same wave vector k_x but opposite frequencies $\pm\omega$, so their profiles oppositely propagate along x . The wave with the largest (smallest) amplitude propagates in the direction of increasing (decreasing) x . At the time of maximum amplitude the two waves are in phase, while they are out of phase by π when the amplitude of δB_z is minimum. To prove this interpretation we considered the following analytical expression:

$$b(x, t) = A_1 \sin [k_x x - \omega(t - t_0) + \phi_1] - A_2 \sin [k_x x + \omega(t - t_0) + \phi_2] \quad (14)$$

that represents the two waves propagating in the opposite directions, and we tried to choose the free parameters in the above expression in a way to reproduce the time evolution of the δB_z profile. In Figure 5 (right) the function $b(x, t)$ is plotted at the same time as in Figure 5 (left), for the following values of the parameters: $A_1 = 6.5 \times 10^3$, $A_2 = 2.5 \times 10^{-3}$, $\omega = 1.2$, $\phi_1 = -(2/3)\pi$, $\phi_2 = \pi/3$, and $t_0=13$. By comparing the two panels of Figure 5, we can see that $b(x, t)$ reproduces remarkably well the time evolution of the δB_z profile. Then, we conclude that the δB_z perturbation is formed by two opposite propagating waves. The wave with the largest amplitude propagates along x in the same direction as the initial perturbation.

In order to identify these waves, we adopted this procedure. First, we estimated the perpendicular wave number of the δB_z perturbation finding $k_\perp \simeq 6.24$. This means that these waves propagate highly oblique to the direction of the background magnetic field. The angle between the wave vector and the background magnetic field direction (x direction) is $\varphi = \arctan(k_\perp/k_\parallel) \simeq 81^\circ$. Then, by considering $\omega \simeq 1.2$ and $k_\parallel = 1$, we can evaluate the parallel propagation velocity as $v_\parallel = \omega/k_\parallel \simeq 1.2$. We have also computed the perpendicular velocity of propagation of this kind of structures in the following way. We identify the position of the structure in the y direction at time t as $y_m(t) \pm \delta y$, where y_m is the point where δB_z is minimum and $\delta y = 0.1$ is an estimation of the uncertainty of the minimum position; this uncertainty is partially due to the fact that the two opposite-propagating perturbations are not exactly superposed along y . Then, we measure the displacement $\Delta y_m = |y_m(t_1 + \Delta t) - y_m(t_1)|$ of the minimum, where t_1 is the initial time of an oscillation period and Δt is the period duration. Finally, we estimate the perpendicular velocity as $v_\perp = \Delta y_m / \Delta t$ finding the value $v_\perp = (5.32 \pm 2.8) \times 10^{-2}$. The above values found for the parallel v_\parallel and perpendicular v_\perp propagation velocities of the observed structures have been respectively compared with the parallel $v_{g\parallel}$ and perpendicular $v_{g\perp}$ group velocities of propagating modes, derived from the linear HMHD theory. Details on the calculation of the explicit expressions for $v_{g\parallel}$ and $v_{g\perp}$ are given in Appendix A. The two components of the group velocity depend on k_\parallel , k_\perp , and β (equations (A12)–(A16)); for k_\parallel and k_\perp we used the above estimated values, while we used $\beta=2.08$ corresponding to the value of $\beta^{(0)}$ at the position $y=5$ where the considered perturbations are localized. The corresponding values of the ω and of the group velocities $v_{g\parallel}$ and $v_{g\perp}$ calculated

Table 2. Frequency ω , Group Velocities $v_{g\parallel}$ and $v_{g\perp}$, and Parallel Phase Velocity $v_{\phi\parallel} = \omega/k_{\parallel}$, for $k_{\parallel} = 1, k_{\perp} = 6.24, \beta = 2.08$, for Kinetic Alfvén Wave (KAW), Fast Magnetosonic (FM), and Slow Magnetosonic (SM) Waves^a

	ω	$v_{g\parallel}$	$v_{g\perp}$	$v_{\phi\parallel}$
KAW	1.30	1.31	0.066	1.30
FM	11.0	0.23	1.74	11.1
SM	0.062	0.62	-0.032	0.62

^aThe velocity values are normalized to the local Alfvén velocity.

by equations (A12)–(A16) are given in Table 2. We can see that the parallel and perpendicular propagation velocities, along with the value of the frequency ω , are in agreement with the values predicted by linear theory for KAW. It is also important to notice that the estimated values of ω, v_{\parallel} , and v_{\perp} are very different from the corresponding values obtained from the linear theory for the Fast Magnetosonic (FM) and Slow Magnetosonic (SM) modes. For example, the FM velocity in the perpendicular direction would be much greater, and the SM velocity would be directed in the opposite direction. Then, the observed localized structure behaves as a KAW, as long as frequency and propagation velocities are concerned.

A further evidence concerning the nature of this perturbation can be deduced on the base of the magnetic field polarization. In Figure 6 we have plotted a hodogram of the perturbation, where the two components δB_x and δB_z are plotted as functions of y . We selected these two components because they are almost transverse to the wave vector orientation, which is almost aligned in the y direction. The hodogram shows that the magnetic field in the considered perturbation turns clockwise when moving in the wave vector direction. On the other hand, from the linear theory (see Appendix A) we can deduce that the magnetic field perturbation is elliptical and it turns clockwise for KAW and FM waves, while it turns counterclockwise for SM waves. Then, the sense of polarization of the localized $\delta B_x - \delta B_z$ perturbation is consistent with that of a KAW.

Based on the above considerations, we conclude that this perturbation may be meaningfully described as a KAW. In particular, this perturbation contains two distinct KAWs, with amplitudes of the same order, which propagate in opposite directions along x but drift in the same direction along y . This condition can be obtained assuming that the two KAWs have the same parallel wave number k_{\parallel} , opposite frequency ω , and opposite perpendicular wave vector k_{\perp} . In fact, from equations (A1)–(A4) we see that the dispersion relation does not change under the transformation $k_{\perp} \rightarrow -k_{\perp}$. Moreover, from equations (A12)–(A16) we see that $v_{g\parallel}$ changes sign and $v_{g\perp}$ remains unchanged under the transformation $k_{\perp} \rightarrow -k_{\perp}, \omega \rightarrow -\omega$. Finally, we note that from equations (A8) and (A10), the sense of polarization remains unchanged under the above transformation; then, we can deduce that the two KAWs forming the considered perturbation have the same sense of polarization.

In conclusion, the simulation shows that in the configuration we have examined that KAWs are formed from the initial Alfvénic perturbation. This happens even in this case in which phase mixing is not present. Since the equilibrium structure is not homogeneous in the perpendicular direction, there is a coupling between

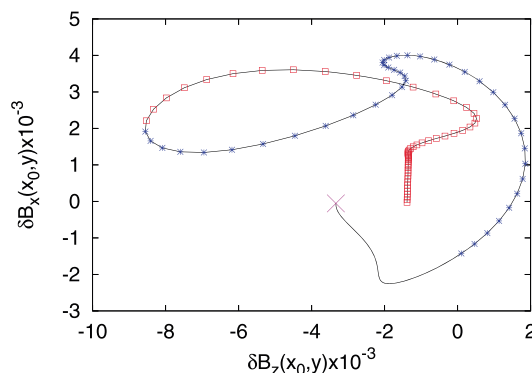


Figure 6. Hodogram of δB_z and δB_x for $\pi \leq y \leq 2\pi$ at $x = \pi$ and $t = 13.0$ (black line). The purple cross indicates the value at $y = \pi$, shear region values are plotted with blue asterisks, and out of shear values with red squares (RUN 1).

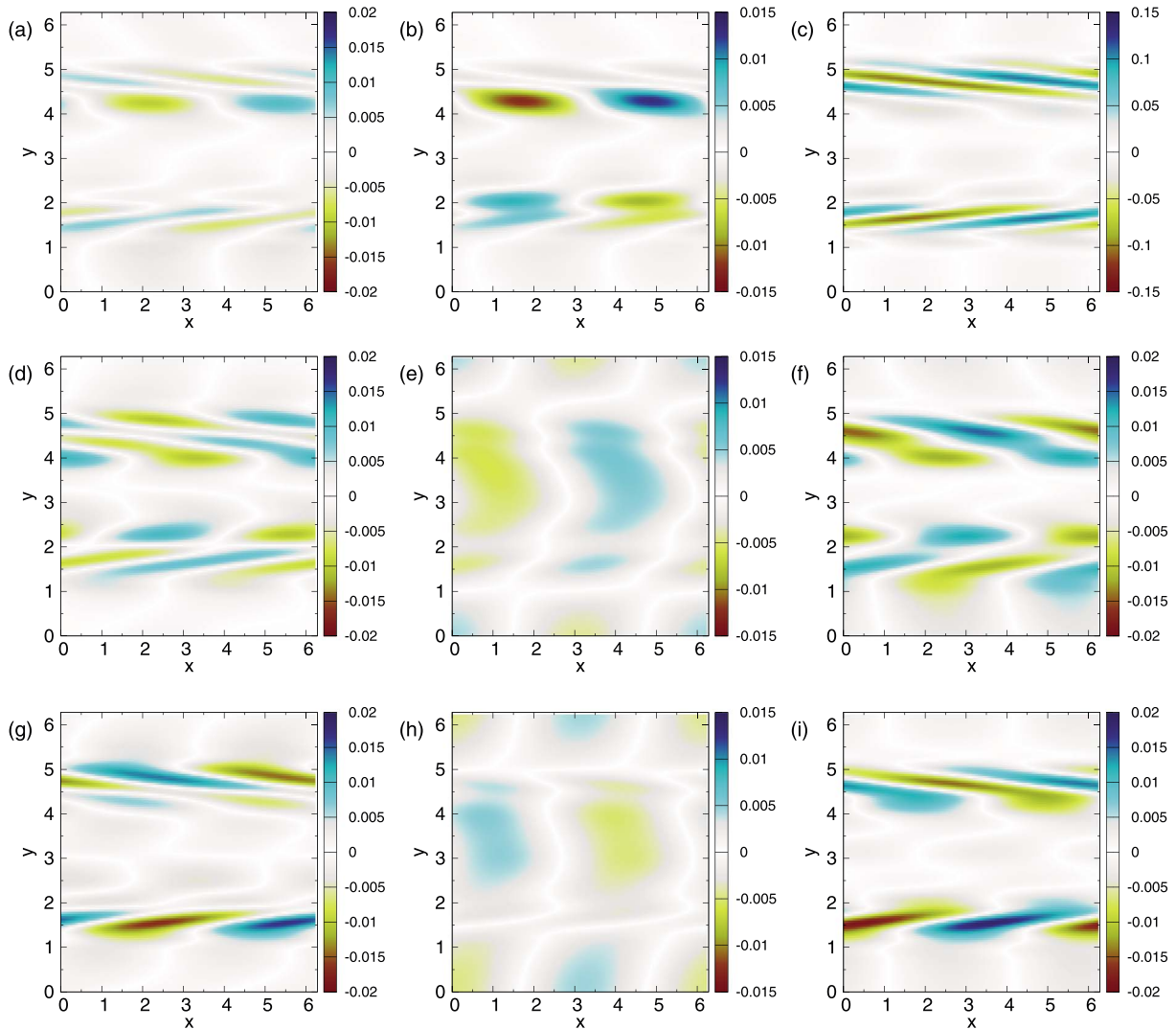


Figure 7. Contour plots of (a) $\delta\rho$; (b) δT ; (c) δj_z ; (d) δv_x ; (e) δv_y ; (f) δv_z ; (g) δB_x ; (h) δB_y ; and (i) δB_z at time $t = 15.0$ (RUN 2).

the initial perturbation with wave vector k_x with a k_y associated with the equilibrium structure. This is also confirmed by the fact that the estimated k_{\perp} of the KAW is of the order of $2\pi/\Delta y_s$ where Δy_s is the size of the shear layers.

3.2. HMHD Simulation in the Out-of-Plane $\mathbf{B}^{(0)}$ Case

Now we discuss the results obtained in RUN 2. Comparing with the case of RUN 1 where equilibrium magnetic field was aligned with the initial wave vector, in this new configuration $\mathbf{B}^{(0)}$ is oriented with an angle of $\pi/4$ with respect to the initial \mathbf{k} , while the initial perturbation is still linearly polarized in the y direction, perpendicular to both $\mathbf{B}^{(0)}$ and \mathbf{k} . In this respect, the initial perturbation is an Alfvén wave. The fluctuations of the various quantities at time $t = 15$ for this run are plotted in Figure 7. The most evident difference with respect to the previous case is that in this case phase mixing is recovered. This can be seen looking, for example, at δB_x and δB_z component (see Figures 7g and 7i), whose structure is progressively stretched in the shear regions. This process is slower than what is observed in the simulation by *Vásconez et al.* [2015] since the in-plane Alfvén velocity is smaller, due to the x component of $\mathbf{B}^{(0)}$ that is now reduced by a factor $\cos \pi/4$. Another particular feature of this configuration is that the evolution is not symmetrical any more with respect to the line $y = \pi$. This lack of symmetry is a consequence of the nonvanishing $B_z^{(0)}$ component. In fact, considering the linearized HMHD equations in the case of in-plane $\mathbf{B}^{(0)}$ ($\theta = 0$), and calculating all the terms on the RHSs of equations (2)

Table 3. Frequency ω , Group Velocities $v_{g\parallel}$ and $v_{g\perp}$, and Parallel Phase Velocity $v_{\phi\parallel} = \omega/k_{\parallel}$, for $k_{\parallel} = \sqrt{2}/2$, $k_{\perp} = 9.94$, $\beta = 1.25$, for Kinetic Alfvén Wave (KAW), Fast Magnetosonic (FM), and Slow Magnetosonic (SM) Waves^a

	ω	$v_{g\parallel}$	$v_{g\perp}$	$v_{\phi\parallel}$
KAW	0.96	1.47	0.047	1.36
FM	14.88	0.11	1.49	21.04
SM	0.36	0.51	-0.016	0.51

^aThe velocity values are normalized to the local Alfvén velocity.

and (3) at the initial time, it is found that each component of the RHS has a well-defined symmetry (symmetrical or antisymmetrical) with respect to the line $y = \pi$. But this property does not hold anymore if $\theta \neq 0$. This explains why the results in the configuration corresponding to RUN 2 are not symmetric.

Similar as in the previous case, a localized perturbation in the x and z components of velocity and magnetic field perturbation develops in the two shear layers. In this case, such perturbations appear to be progressively stretched along an oblique direction, due to phase mixing, so that the perpendicular wave vector tends to increase until it becomes of the order of $\tilde{\epsilon}^{-1}$. We characterized the nature of the fluctuations that arise in the two shear regions. First, we estimated the value of the perpendicular wave vector as $k_{\perp} = 9.94$ at the time instant $t = 15$. Then we estimated the velocity of propagation in parallel and perpendicular directions. We did it through a similar approach as that used for RUN 1. We identified the minimum of δB_z in the space region where $4.0 < y < 5.0$ and followed its position for five computational times. Then, we linearly interpolated the x and y components of the position of the minimum as functions of time, finding the following two values for the propagation velocity along the x and y directions: $v_x = 0.8$ and $v_y = 2.2 \times 10^{-2}$. In order to compare these velocities with the predictions of the linear theory, the specific geometry of this configuration has to be taken into account. The background magnetic field direction is given by $\hat{\mathbf{e}}_B = \cos \theta \hat{\mathbf{e}}_x + \sin \theta \hat{\mathbf{e}}_z$ and the direction of the wave vector is given by $\hat{\mathbf{k}} = (k_x \hat{\mathbf{e}}_x + k_y \hat{\mathbf{e}}_y)/k$, where $k = \sqrt{k_x^2 + k_y^2}$. From the previous two equations we get $k_{\parallel} = k_x \cos \theta$ and, using the condition $k_y \gg k_x$, we can make the following approximation $k_{\perp} \simeq k_y$. Hence, the estimated velocities are $v_{\parallel} = v_x / \cos \theta \simeq 1.12$ and $v_{\perp} \simeq v_y \simeq 2.2 \times 10^{-2}$. By comparing these values with the linear modes group speeds $v_{g\parallel}$ and $v_{g\perp}$ (see Table 3), we found that the propagation velocity estimated from the simulation results is compatible with the KAWs group velocity, while it does not agree with the group velocity of FM and SM waves. We remark that the values presented in Table 3 have been calculated using $\beta = 1.25$, which corresponds to the value at the center of the shear layers, where the perturbation is localized.

The hodogram plotted in Figure 8 confirms the interpretation of the observed magnetic fluctuations as KAWs. In fact, it shows a polarization that turns clockwise when moving in the y direction, as expected from linear theory. We can also conclude that in this case the initial large amplitude Alfvén mode is locally converted

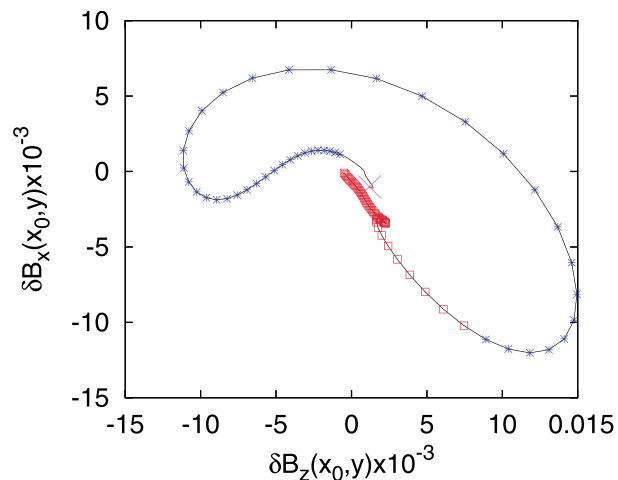


Figure 8. Hodogram of δB_z and δB_x for $\pi \leq y \leq 2\pi$ at $x = \pi$ and $t = 13.0$ (black line). The purple cross indicates the value at $y = \pi$, shear region values are plotted with blue asterisks, and out of shear values with red squares. (RUN 2)

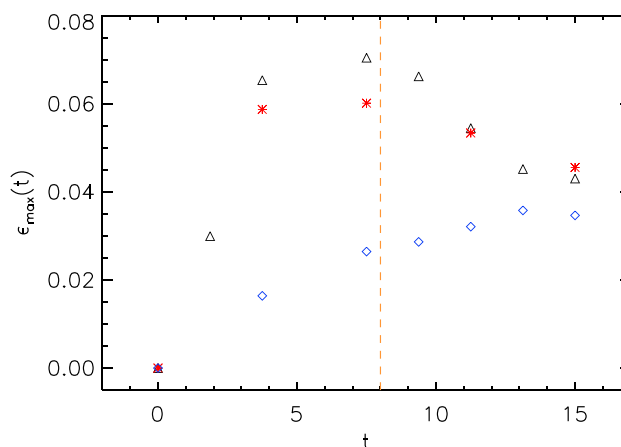


Figure 9. Quantity $\epsilon_{\max}(t)$ plotted as a function of time for Paper I (blue diamonds), RUN 3 (red stars), and RUN 4 (black triangles).

into a KAW; in this case phase mixing plays a role in the formation of small scales. The formation of transverse propagating fast waves is observed also in this case, but this phenomenon is less evident and plays a minor role in the dynamics of the physical system.

3.3. Kinetic Effects

In this section, we show the results of the kinetic simulations for the following cases: in-plane $B^{(0)}$ (RUN 3) and out-of-plane $B^{(0)}$ (RUN 4). As in the HMHD cases, also here small-scale magnetic field fluctuations form in the shear regions. Furthermore, since HVM simulations are nonlinear, the proton VDF f displays

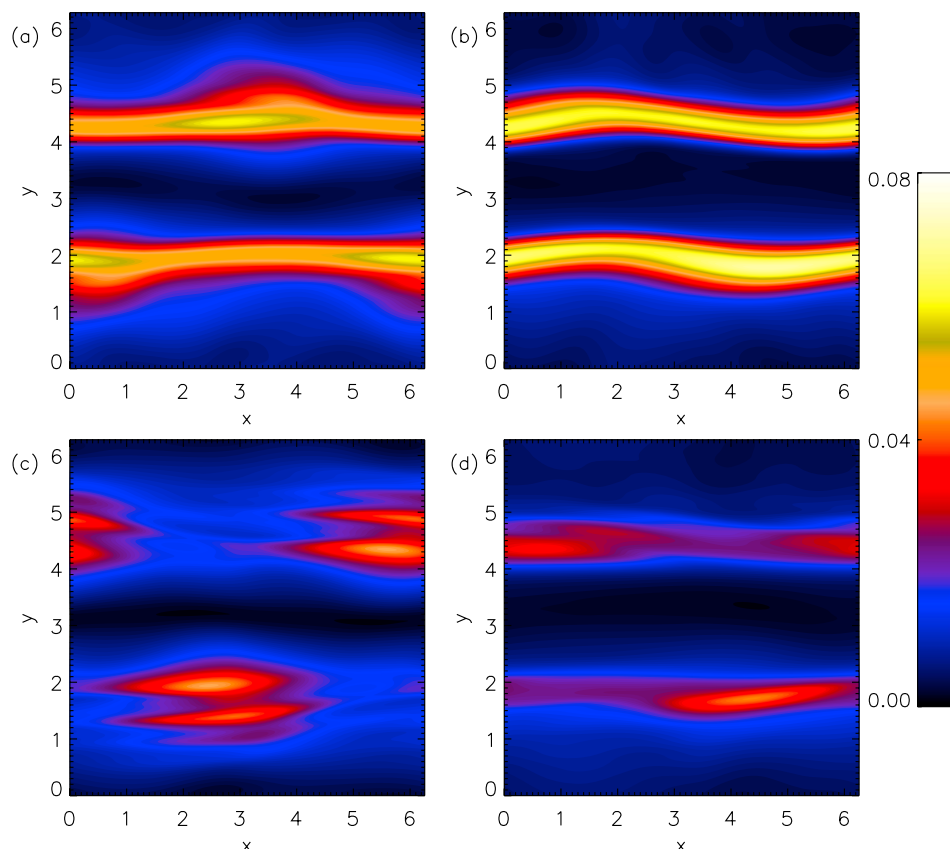


Figure 10. Contour plots of $\epsilon(x, y)$ at time (a, b) $t=7.5$ and (c, d) $t=15$. Left column refers to RUN 3, while right column indicates RUN 4.

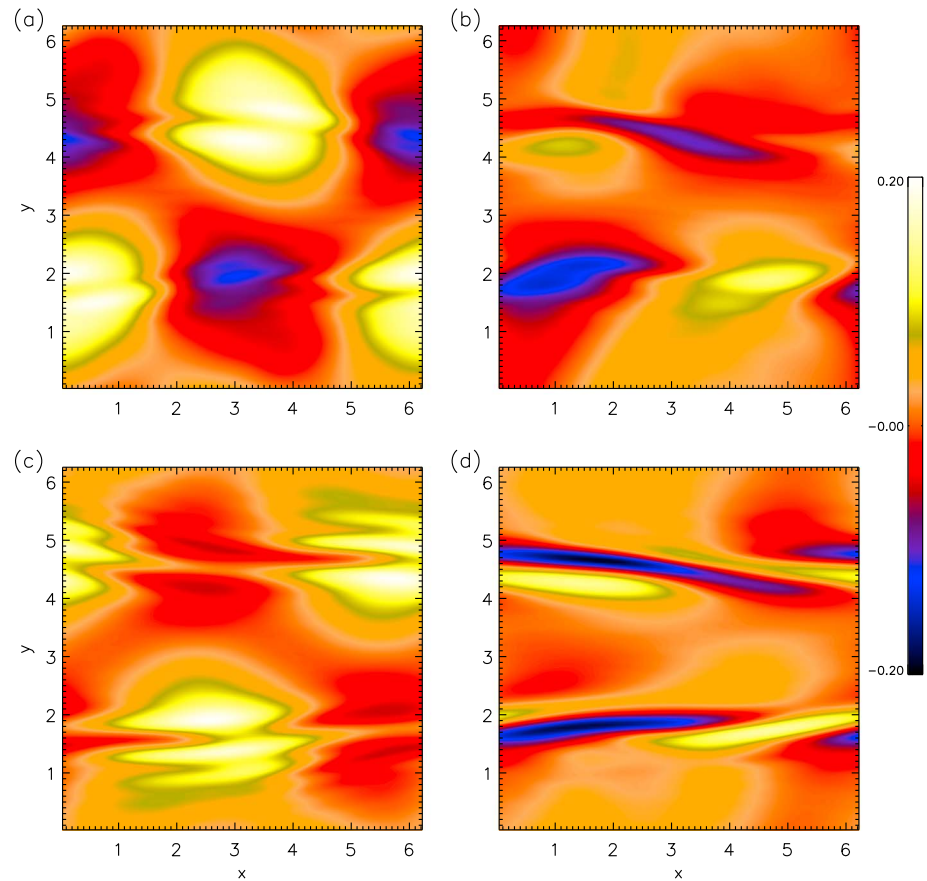


Figure 11. Contour plots of $R(x, y)$ at time (a, b) $t = 7.5$ and (c, d) $t = 15$. Left column refers to RUN 3, while right column indicates RUN 4.

non-Maxwellian features due to wave-particle interactions where these small scales are present. To quantify these deformations, we computed the L^2 norm difference [Greco *et al.*, 2012]:

$$\epsilon(x, y, t) = \frac{1}{n} \sqrt{\int [f(\mathbf{x}, \mathbf{u}, t) - f_M(\mathbf{x}, \mathbf{u}, t)]^2 d^3 \mathbf{u}} \quad (15)$$

where $f_M(\mathbf{x}, \mathbf{u}, t)$ is the Maxwellian distribution function associated with $f(\mathbf{x}, \mathbf{u}, t)$, constructed in a way that density, bulk velocity, and total temperature of the two VDFs are the same. Figure 9 shows the evolution of $\epsilon_{\max}(t = \max_{(x,y) \in D} \epsilon(x, y, t))$ as a function of time. Red stars, black triangles, and blue diamonds, respectively, indicate RUN 3, RUN 4, and, finally, the Paper I case, which has been included in Figure 9 for a better comparison.

In the Paper I case, $\epsilon_{\max}(t)$ smoothly increases and saturates at $\epsilon^{\text{sat}} \simeq 0.035$. On the other hand, in both RUN 3 and RUN 4 cases, $\epsilon_{\max}(t)$ rapidly increases for times $t < t_d \simeq 8$ (indicated in Figure 9 by an orange dashed line) reaching values about two times bigger than ϵ^{sat} . Then, for $t > t_d$ it decreases and finally approaches a value comparable with ϵ^{sat} . We remark that t_d is the time necessary for the phase-mixing process to form transverse wave vectors comparable with \tilde{d}_p^{-1} in the Paper I configuration.

As in Paper I, KAW-like fluctuations produce modifications of the VDFs in both RUN 3 and RUN 4 cases. However, both the new cases of study suggest the presence of a transient period in which kinetic effects are stronger than that found in Paper I. In order to characterize the nature of this transient and the nature of the asymptotic behavior, we analyze in detail two time instants: (i) $t = 7.5 = 60\Omega_{\text{cp}}^{-1}$, which corresponds to the time where $\epsilon_{\max}(t) = \max_t \epsilon_{\max}(t)$ and (ii) that $t = 15 = 120\Omega_{\text{cp}}^{-1}$, which is the final instant of the simulation.

Figure 10 shows the 2-D contour plots of $\epsilon(x, y)$ at $t = 7.5$ (Figures 10a and 10b) and $t = 15$ (Figures 10c and 10d) as a function of x and y for the two runs. The intensity of $\epsilon(x, y)$ is slightly smaller in the RUN 3 case compared

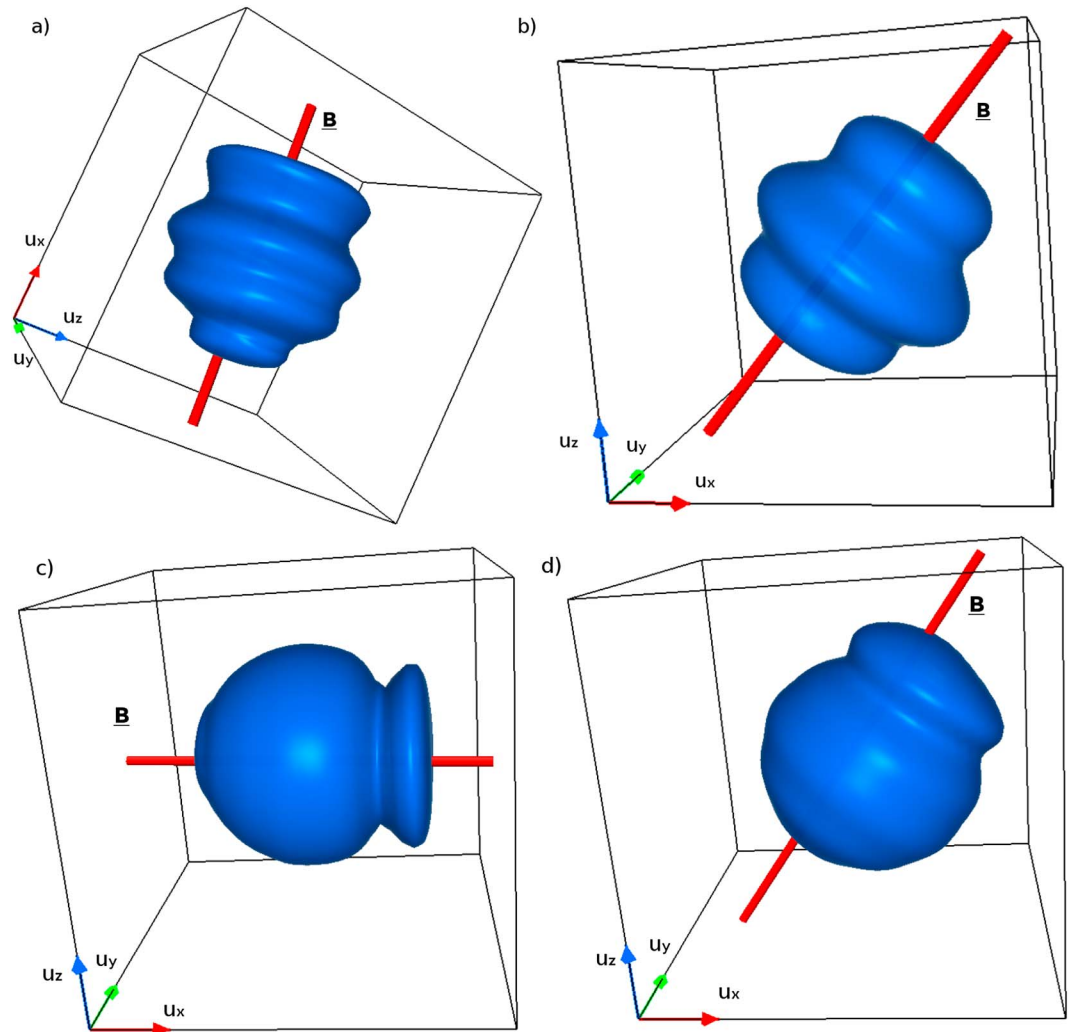


Figure 12. Three-dimensional isosurface plot of the VDFs at time (a, b) $t = 7.5$ and (c, d) $t = 15$, where ϵ is maximum. Left column refers to RUN 3, while right column indicates RUN 4.

with the RUN 4 case. Moreover, the $\epsilon(x, y)$ shape is more structured in the RUN 3 case than in the RUN 4 case. Indeed in the in-plane $B^{(0)}$ case (RUN 3), at both $t = 7.5$ (Figure 10a) and $t = 15$ (Figure 10c), $\epsilon(x, y)$ presents some ripples toward the external sides of the y domain. These deformations are clearly visible at $t = 15$ (Figure 10c) where at least two strong regions of non-Maxwellianity are recovered. On the other hand, in the out-of-plane $B^{(0)}$ case (RUN 4), the region where $\epsilon(x, y)$ is significantly not null is more uniform and confined within the shear. Moreover, for both RUN 3 and RUN 4 cases, $\epsilon(x, y)$ is not zero in two slab-like regions at $t = 7.5$ (see Figures 10a and 10b), while, at $t = 15$ (see Figures 10c and 10d), it is concentrated into bubble-like areas. We suggest the following interpretation for these features: at $t = 7.5$ the large amplitude initial perturbation is interacting with the background structure modifying the VDFs in the shear layer. This interaction gives rise to the formation of KAWs that at later times remain the main factors responsible for the deformations of the VDFs. Indeed, the regions where the distribution function departs from Maxwellian at $t = 15$ are the regions in which KAWs are identified.

Departures of the proton distribution function from the Maxwellian form can be also identified with the temperature anisotropy index [Perrone et al., 2014], $R(x, y, t) = 1 - T_{\perp L}(x, y, t)/T_{\parallel L}(x, y, t)$, $T_{\perp L}$, and $T_{\parallel L}$ being, respectively, the proton perpendicular and parallel temperatures evaluated with respect to the local magnetic field \mathbf{B} . Figure 11 shows instantaneous spatial distribution of $R(x, y)$ at $t = 7.5$ (Figures 11a and 11b) and at $t = 15$ (Figures 11c and 11d); corresponding to RUN 3 (Figures 11a and 11c) and RUN 4 (Figures 11b and 11d). This figure confirms a previous result of Paper I: KAWs produce both $R > 0$ and $R < 0$ regions, corresponding

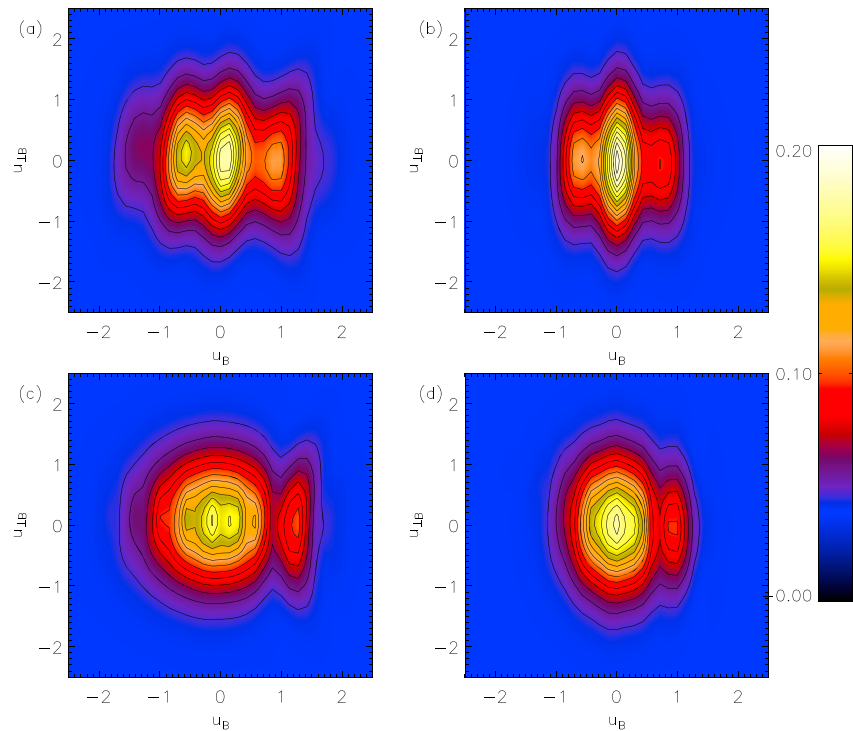


Figure 13. Two-dimensional isosurface plot of the VDFs at time (a, b) $t = 7.5$ and (c, d) $t = 15$, where ϵ is maximum and in the plane $u_B - u_{\perp B}$. Left column refers to RUN 3, while right column indicates RUN 4.

to anisotropic VDFs in the parallel and perpendicular directions. A clear correlation between the kinetic deformations of f and the spatial distribution of the index R is recovered, and both the parameters R and ϵ recall the shape of the magnetic field fluctuations (see Figures 4i and 7i).

In order to display the effects of wave-particle resonances on the distribution function, we present in Figure 12 the 3-D isosurface plots of the VDFs for $t = 7.5$ (Figures 12a and 12b) and $t = 15$ (Figures 12c and 12d) taken at the spatial point where ϵ is maximum. Figures 12a and 12c refer to RUN 3, while Figures 12b and 12d refer to RUN 4. In all cases, VDFs are clearly gyrotropic with respect to the local magnetic field. Moreover at $t = 7.5$ VDFs present deformations toward both positive and negative velocities (see Figures 12a and 12b), while, at $t = 15$, a single beam is present in the positive velocity direction (see Figures 12c and 12d). At this time, the shapes of the VDFs are similar to those described in Paper I, e.g., rings perpendicular to the direction of local magnetic field and a beam directed in the parallel direction.

In order to single out the VDFs non-Maxwellian features, we show in Figures 13a–13d the 2-D contour plots of the VDFs in the plane $u_B - u_{\perp B}$, u_B and $u_{\perp B}$ being, respectively, the parallel and perpendicular directions with respect to the local magnetic field, in the velocity space. We remark that the VDFs shown in Figures 13a–13d are the same as those shown in Figures 12a–12d. At $t = 7.5$ (Figures 13a and 13b) two beam-like deformations are recovered in the VDFs for both positive and negative velocities. On the other hand, at $t = 15$ (Figures 13c and 13d), a single proton beam is recovered in the distribution function shape in the direction parallel to \mathbf{B} .

Beam velocities ($v_b \approx 1.3$ for RUN 3 and $v_b \approx 1.0$ for RUN 4) are in good agreement with the estimated KAWs parallel propagation velocities in the corresponding HMHD linear simulations, suggesting particle resonances with these fluctuations. In our simulation the formation of a beam is related to the fluctuating parallel electric field δE_{\parallel} associated with the KAWs. In fact, Ohm's law (equation (6)) allows for the presence of an electric field component $E_{\parallel} = \mathbf{E} \cdot \mathbf{B}/B$ parallel to the local magnetic field due to the electron pressure gradient. The typical values of these fluctuations in the region where KAWs are localized are of the order $\delta E_{\parallel} \sim 10^{-2}$. In the ideal HMHD case, E_{\parallel} has no effect on the dynamics (the term containing $\nabla P_e/n$ being canceled out when calculating $\nabla \times \mathbf{E}$), unless one also includes resistivity. However, in the HVM model, it can have an influence on the evolution of the proton distribution function. If we consider the potential energy variation (per particle)

δU associated with δE_{\parallel} and the proton thermal energy E_{th} , the ratio between these two quantities, expressed in our normalized units, can be estimated as follows:

$$\frac{\delta U}{E_{\text{th}}} \sim \frac{8}{3\tilde{\epsilon}\tilde{\beta}} \frac{\delta E_{\parallel}\lambda_{\parallel}}{T_p}, \quad (16)$$

where λ_{\parallel} is the parallel wavelength and T_p is the proton temperature. Using the values $\tilde{\epsilon} = 0.125$, $\tilde{\beta} = 2$, $\delta E_{\parallel} \sim 10^{-2}$, $\lambda_{\parallel} = 2\pi$, and $T_p \sim 0.5$, from equation (16) we find $\delta U/E_{\text{th}} \sim 1$. Then, the potential energy variation due to the parallel electric field associated with KAWs is comparable to the proton thermal energy, implying that KAW δE_{\parallel} is able to sensibly modify the initial proton distribution function.

The role of the electron equation of state on the proton distribution function evolution is still on debate. In these hybrid kinetic simulations electrons are an isothermal fluid, with temperature equal to the initial proton temperature. As shown above, the parallel electric field component, due to the electron pressure gradient term, is responsible for protons acceleration in the parallel direction and changes proportionally to the electron specific heat ratio (5/3 or 1 for the adiabatic or isothermal case, respectively). For this reason, an adiabatic equation of state for electrons might produce stronger kinetic effects with respect to the isothermal electrons case. This has been actually reported in hybrid simulations of turbulence [Parashar *et al.*, 2014]. However, the comparison of the HMHD and HVM models in Paper I, in a system quite analogous to the one here analyzed, suggested that the two models, despite having different closures for electrons, produce similar results. Hence, in this case, the kinetic dynamics and, in particular, the process of beam formation might be qualitatively similar in the isothermal and adiabatic cases.

4. Conclusions

In this paper we have studied the evolution of an initial Alfvénic perturbation propagating in an inhomogeneous equilibrium pressure-balanced structure, in which the equilibrium quantities vary in a direction (y) perpendicular to the magnetic field $\mathbf{B}^{(0)}$ orientation. Dispersive and kinetic effects have been included using a HMHD and a HVM numerical model, respectively. A similar problem has been already studied (Paper I) in a particular case in which the initial perturbation wave vector \mathbf{k}_0 is parallel to $\mathbf{B}^{(0)}$ and the initial polarization is perpendicular both to $\mathbf{B}^{(0)}$ and to the inhomogeneity y direction. In the present paper we have generalized the results of Paper I, considering two different initial conditions: in the first case (in-plane $\mathbf{B}^{(0)}$), \mathbf{k}_0 is parallel to $\mathbf{B}^{(0)}$, but the polarization is along the inhomogeneity direction; in the second case (out-of-plane $\mathbf{B}^{(0)}$), \mathbf{k}_0 is at an angle $\theta = \pi/4$ with $\mathbf{B}^{(0)}$, and the wave is polarized in the direction perpendicular to both \mathbf{k}_0 and $\mathbf{B}^{(0)}$, which coincides again with the inhomogeneity y direction. Both configurations are inherently different from that considered in Paper I; in fact, during the time evolution, the coupling between the perturbation and the background inhomogeneity makes the local wave vector \mathbf{k} to increase and rotate toward the y direction. Then, in both cases considered here, the initial polarization is no longer perpendicular to \mathbf{k} with increasing time. This generates compressive fluctuations in the shear regions, whose amplitude is of the same order as the initial Alfvénic perturbation. In contrast, in the case considered in Paper I, the polarization remains perpendicular to \mathbf{k} ; i.e., the perturbation remains noncompressive, at least until the wave vector \mathbf{k} becomes large enough to make dispersive effects no longer negligible.

In the Paper I configuration, the results have shown that in the shear regions the initial Alfvén wave is subject to phase mixing that gradually transforms such a perturbation into a KAW. One of the aims of this study is to verify whether KAWs are generated also in the newly considered configurations. In the in-plane $\mathbf{B}^{(0)}$ case, no phase mixing has been found, similar to what has been observed in a purely MHD case [Malara *et al.*, 1996]; nevertheless, we have found the formation of KAWs in the shear regions. KAWs have been identified both comparing their propagation velocity with the group velocity of dispersive modes and by considering their polarization. However, the transverse wavelength λ_{\perp} of these perturbations is of the order of the shear layer width $2\pi h \sim 1$; i.e., it is slightly larger than those found in Paper I. This indicates that a coupling between the initial wave and the background inhomogeneity, different from phase mixing, is responsible for the KAW formation in this case. In our simulations the proton inertial length is $d_p = 0.125$ (in normalized units), so that $k_{\perp}d_p = 2\pi d_p/\lambda_{\perp} \sim d_p/h \simeq 0.6$, so that the perpendicular wavelength is comparable with d_p ; this explains why dispersive effects, which characterize KAWs, play a major role in the observed dynamics. However, in a case where the proton inertial length were much smaller than the shear width, it remains unclear whether KAWs would form in the in-plane $\mathbf{B}^{(0)}$ configuration. In the out-of-plane $\mathbf{B}^{(0)}$ case, we observed that the perturbation

is subject to phase mixing, which generates fluctuations in the shear layers at scales even smaller than the shear layer width. Also in this case, such fluctuations have been identified as KAWs. The most general initial configuration for a linearly polarized Alfvén wave can be considered as a linear combination of the three cases here discussed. Then, we conclude that when an Alfvén wave propagates in transverse inhomogeneous structures, KAWs are eventually produced regardless of the initial wave polarization and of the propagation angle θ .

The large-amplitude simulations performed by the HVM model have shown that at KAW locations the proton distribution function is progressively modified with respect to the initial Maxwellian. Temperature anisotropies are generated, with $T_{\parallel} > T_{\perp}$ or the reverse, according to the phase of the KAW. The shape of the distribution function reveals resonant wave-particle interactions. At locations where T_{\parallel} is particularly large, a beam of ions moving along the magnetic field in the propagation direction of the initial wave is observed.

These results have been derived within a simplified context, where it is possible to distinguish between a single well-defined wave and the inhomogeneous background. However, some indications about the possibility of generating KAWs in more complex situations, like in turbulence, can be deduced. In fact, the wave-inhomogeneity coupling considered in this study is of a similar nature as the nonlinear coupling between fluctuations which generates the turbulent cascade in MHD: the phenomenon we studied is closely related to the mechanism that favors perpendicular spectral transfer in the nonlinear cascade [Shebalin *et al.*, 1983]. Then, our results give a positive indication about the possibility to generate KAW-like fluctuations at proton scales within a turbulent cascade, as suggested by solar wind observations [Bale *et al.*, 2005; Sahraoui *et al.*, 2012].

Appendix A: Linear Waves in Hall MHD

This appendix is devoted to describe the main feature of the linear waves that are normal modes in Hall MHD. We start from equations (1)–(4) and consider a homogeneous plasma with dimensionless density ρ_0 and temperature T_0 , which are permeated by a homogeneous magnetic field \mathbf{B}_0 . The plasma is at rest at the beginning: $\mathbf{v}_0 = 0$. We perturb this equilibrium structure with a small-amplitude fluctuation and linearize the equations getting equations for the fluctuations. Then we write the unknown fluctuations as a superposition of plane waves and we get the equation for the fluctuation amplitudes. Imposing nonvanishing amplitudes leads to an equation of this type:

$$\omega^6 + C_1\omega^4 + C_2\omega^2 + C_3 = 0 \quad (\text{A1})$$

with

$$C_1 = -k_{\parallel}^2 (2c_{A0}^2 + c_{s0}^2) - k_{\perp}^2 (c_{A0}^2 + c_{s0}^2) - \frac{c_{A0}^4 k_{\parallel}^2 (k_{\parallel}^2 + k_{\perp}^2)}{\omega_{p0}^2} \quad (\text{A2})$$

$$C_2 = c_{A0}^2 k_{\parallel}^2 (c_{A0}^2 + 2c_{s0}^2) (k_{\parallel}^2 + k_{\perp}^2) + \frac{c_{A0}^4 c_{s0}^2 k_{\parallel}^2 (k_{\parallel}^4 + 2k_{\parallel}^2 k_{\perp}^2 + k_{\perp}^4)}{\omega_{p0}^2} \quad (\text{A3})$$

$$C_3 = -c_{A0}^4 c_{s0}^2 k_{\parallel}^4 (k_{\parallel}^2 + k_{\perp}^2) \quad (\text{A4})$$

In equations (A1)–(A4), k_{\parallel} and k_{\perp} are the wave vector components parallel and perpendicular to \mathbf{B}_0 , respectively, normalized to a typical length \tilde{L} ; $c_{A0} = B_0/(4\pi\rho_0)^{1/2}$ and $c_{s0} = (\tilde{\beta}\gamma T_0/2)^{1/2}$ are the Alfvén and sound speed associated with the equilibrium structure, respectively, where $\tilde{\beta}$ is the typical ratio between the kinetic and magnetic pressure; ω is the frequency normalized to $\tilde{\tau}_A^{-1} = \tilde{L}/\tilde{c}_{A0}$, and $\omega_{p0} = (q\tilde{B}B_0/(m_p c))(\tilde{L}/\tilde{c}_A)$ is the normalized proton gyrofrequency. The expressions (A1)–(A4) are equivalent to what was found by Vasconez *et al.* [2014] in a two-fluid model if the electron inertia is neglected. Equation (A1) has been analytically solved [Vasconez *et al.*, 2014] using the Vieta's substitution method [Birkhoff and MacLane, 1977] for the calculation of the complex roots of a third-degree algebraic equation. For given values of k_{\parallel} and k_{\perp} three real and positive solutions are found for ω^2 , corresponding to the Alfvén, fast magnetosonic (FM), and slow magnetosonic (SM) branches, respectively. In particular, KAWs correspond to the Alfvén branch for $k_{\parallel} \ll k_{\perp} \sim \omega_{p0}/c_{A0}$.

It is possible to calculate the expression of the fluctuation amplitudes from linear analysis. If a reference frame is considered where the x axis is along \mathbf{B}_0 and the wave vector \mathbf{k} is in the xy plane, the perturbation components for a wave with wave vector $\mathbf{k} = k_{\parallel}\mathbf{e}_x + k_{\perp}\mathbf{e}_y$ can be expressed in the following form:

$$v_{1x} = a \frac{c_{A0}^2 c_{s0}^2 k_{\parallel}^2 k_{\perp} \omega_{p0}}{\omega^2 (\omega^2 - c_{s0}^2 k^2)} \left(1 - \frac{\omega^2}{c_{A0}^2 k_{\parallel}^2} \right) \sin(k_{\parallel}x + k_{\perp}y - \omega t + \phi) \quad (\text{A5})$$

$$v_{1y} = a \frac{c_{A0}^2 k_{\parallel} \omega_{p0} (\omega^2 - c_{s0}^2 k_{\parallel}^2)}{\omega^2 (\omega^2 - c_{s0}^2 k^2)} \left(1 - \frac{\omega^2}{c_{A0}^2 k_{\parallel}^2} \right) \sin(k_{\parallel}x + k_{\perp}y - \omega t + \phi) \quad (\text{A6})$$

$$v_{1z} = -a \frac{c_{A0}^2 k_{\parallel}}{\omega} \cos(k_{\parallel}x + k_{\perp}y - \omega t + \phi) \quad (\text{A7})$$

$$B_{1x} = aB_0 \frac{k_{\parallel} k_{\perp} \omega_{p0}}{\omega k^2} \left(1 - \frac{\omega^2}{c_{A0}^2 k_{\parallel}^2} \right) \sin(k_{\parallel}x + k_{\perp}y - \omega t + \phi) \quad (\text{A8})$$

$$B_{1y} = -aB_0 \frac{k_{\parallel}^2 \omega_{p0}}{\omega k^2} \left(1 - \frac{\omega^2}{c_{A0}^2 k_{\parallel}^2} \right) \sin(k_{\parallel}x + k_{\perp}y - \omega t + \phi) \quad (\text{A9})$$

$$B_{1z} = aB_0 \cos(k_{\parallel}x + k_{\perp}y - \omega t + \phi) \quad (\text{A10})$$

where a is the perturbation amplitude, $\phi \in [0, 2\pi]$ is the phase, and $\omega = \omega(\mathbf{k})$ is derived from the dispersion relation (A1). From (A1) it is also possible to find the expression for the parallel and perpendicular group velocities. We consider equation (A1) written in the implicit form:

$$F(\omega(k_{\parallel}, k_{\perp}), k_{\parallel}, k_{\perp}) \equiv 0, \quad (\text{A11})$$

which holds for any value of k_{\parallel} and k_{\perp} . The total derivative of equation (A11) with respect to k_{\parallel} is

$$\frac{dF}{dk_{\parallel}} = \frac{\partial F}{\partial \omega} \frac{\partial \omega}{\partial k_{\parallel}} + \frac{\partial F}{\partial k_{\parallel}} = 0$$

from which we obtain

$$v_{g\parallel} = \frac{\partial \omega}{\partial k_{\parallel}} = -\frac{\partial F / \partial k_{\parallel}}{\partial F / \partial \omega}. \quad (\text{A12})$$

where $v_{g\parallel}$ is the parallel group velocity. In a similar way we obtain the perpendicular group velocity

$$v_{g\perp} = \frac{\partial \omega}{\partial k_{\perp}} = -\frac{\partial F / \partial k_{\perp}}{\partial F / \partial \omega}. \quad (\text{A13})$$

The derivatives of F appearing in equations (A12) and (A13) calculated by using equation (A1) are

$$\begin{aligned} \frac{\partial F}{\partial k_{\parallel}} = & 2 \left[k_{\parallel} (2c_{A0}^2 + c_{s0}^2) + \frac{c_{A0}^2}{\omega_{p0}^2} (2k_{\parallel}^3 + k_{\parallel} k_{\perp}^2) \right] \omega^4 \\ & + 2 \left[(2c_{s0}^2 c_{A0}^2 + c_{A0}^4) (2k_{\parallel}^3 + k_{\parallel} k_{\perp}^2) + \frac{c_{A0}^4 c_{s0}^2}{\omega_{p0}^2} (3k_{\parallel}^5 + k_{\parallel}^4 k_{\perp}^2 + k_{\parallel} k_{\perp}^4) \right] \omega^2 \\ & - 2c_{s0}^2 c_{A0}^4 (3k_{\parallel}^5 + 2k_{\parallel}^3 k_{\perp}^2) \end{aligned} \quad (\text{A14})$$

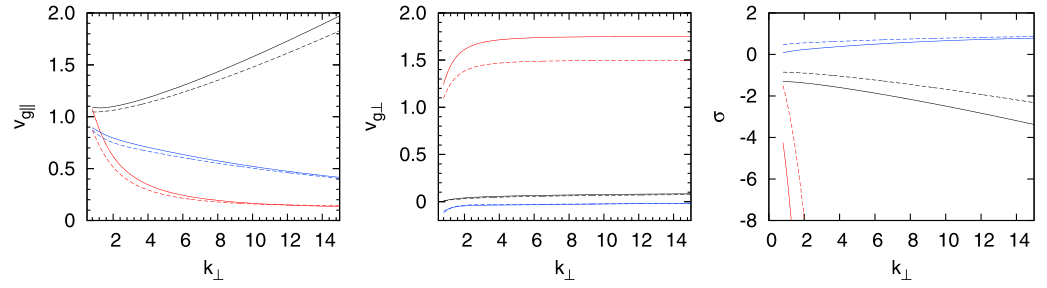


Figure A1. (left) Parallel group velocity, (middle) perpendicular group velocity, and (right) σ as functions of k_{\perp} , for $k_{\parallel} = 1$ (RUN 1). Red lines correspond to Fast mode, black lines to kinetic Alfvén wave, and blue lines to Slow mode. Dashed lines for $\beta = 1.25$, full lines for $\beta = 2.08$.

$$\frac{\partial F}{\partial k_{\perp}} = -2 \left[k_{\perp} (c_{A0}^2 + c_{s0}^2) + \frac{k_{\perp} k_{\parallel}^2 c_{A0}^4}{\omega_{p0}^2} \right] \omega^4 + 2 \left[k_{\perp} k_{\parallel}^2 (2c_{s0}^2 c_{A0}^2 + c_{A0}^4) + 2 \frac{(k_{\perp} k_{\parallel}^4 + k_{\perp}^3 k_{\parallel}^2) c_{A0}^4 c_{s0}^2}{\omega_{p0}^2} \right] \omega^2 - 2k_{\perp} k_{\parallel}^4 c_{s0}^2 c_{A0}^4 \quad (\text{A15})$$

$$\frac{\partial F}{\partial \omega} = 6\omega^5 - 4 \left[k^2 (c_{A0}^2 + c_{s0}^2) + k_{\parallel}^2 c_{A0}^2 + \frac{k^2 k_{\parallel}^2 c_{A0}^2}{\omega_{p0}^4} \right] \omega^3 + 2 \left[k^2 k_{\parallel}^2 (2c_{s0}^2 c_{A0}^2 + c_{A0}^4) + \frac{k_{\parallel}^2 k^4 c_{A0}^4 c_{s0}^2}{\omega_{p0}^2} \right] \omega \quad (\text{A16})$$

where $k^2 = k_{\parallel}^2 + k_{\perp}^2$. Since in the simulation considered in this work fluctuations at large k_{\perp} develop during the system evolution we plotted in Figure A1 the parallel and perpendicular velocities as a function of k_{\perp} for $k_{\parallel} = 1$ and for two different values of β_0 corresponding to the shear and homogeneous side regions of the equilibrium structure considered. We can see that in the parallel direction the group velocities are positive for all the three modes. In particular, parallel group velocity increases with k_{\perp} for KAW and decreases for FM and SM modes. Perpendicular group velocity increases for all the three modes at increasing k_{\perp} rapidly reaching an asymptotic value. It is always positive for KAW and FM and negative for SM. It is worth noting that perpendicular group velocity for FM is much more bigger than for KAW. We notice also that the group velocities are similar for the two values of β_0 considered for all the three modes. Finally, in Figure A1 (right), we plotted the quantity

$$\sigma = 1 - \frac{\omega^2}{c_{A0}^2 k_{\parallel}^2}. \quad (\text{A17})$$

Acknowledgments

The numerical HVM simulations have been running on the Fermi supercomputer at CINECA (Bologna, Italy), within the ISCRA-C projects IsC26-PMKAW and IsC25-MHDwMoPC. C.L. Vásconez was partially supported by SENESCYT-Ecuador 2012-1 Scholarship. This work has been supported by the Agenzia Spaziale Italiana under contract ASI-INAF 2015-039-R.O “Missione M4 di ESA: Partecipazione Italiana alla fase di assessment della missione THOR.” The author would like to thank the anonymous reviewers for their insightful comments and suggestions that have contributed to improve this paper. No data was used in producing this manuscript.

that appears in equations (A5)–(A10). If the condition $k_y \gg k_x$ holds, that in our configuration means $k_{\perp} \gg k_{\parallel}$, $\nabla \cdot \mathbf{B} = 0$ implies that the dominant components of a quasi-oblique fluctuation will be B_{1x} and B_{1z} . Equations (A5)–(A10) indicate that in this case such fluctuation is elliptically polarized. For positive k_{\parallel} and k_{\perp} and given values of t and x , as one increases the y coordinate, the perturbation magnetic field rotates clockwise (counterclockwise) in the zx plane for negative (positive) values of σ . Since the sign of σ is unique for the three modes, positive for SM and negative for KAW and FM, the polarization of the magnetic field perturbation can be used, along with information about group velocity, to distinguish one mode from the other.

References

- Araneda, J. A., E. Marsch, and A. F-Viñas (2008), Proton core heating and beam formation via parametrically unstable Alfvén-cyclotron waves, *Phys. Rev. Lett.*, *100*(12), 125003.
- Bale, S., P. Kellogg, F. Mozer, T. Horbury, and H. Reme (2005), Measurement of the electric fluctuation spectrum of magnetohydrodynamic turbulence, *Phys. Rev. Lett.*, *94*(21), 215002.
- Belcher, J., and L. Davis (1971), Large-amplitude Alfvén waves in the interplanetary medium, *J. Geophys. Res.*, *76*(16), 3534–3563.
- Birkhoff, G., and S. MacLane (1977), *A Survey of Modern Algebra*, McGraw-Hill, New York.
- Bruno, R., and V. Carbone (2005), The solar wind as a turbulence laboratory, *Living Rev. Sol. Phys.*, *2*, 4, doi:10.12942/lrsp-2005-4.

- Califano, F., C. Chiuderi, and G. Einaudi (1990), Nonresonant resistive dissipation of incompressible magnetohydrodynamic waves, *Astrophys. J.*, *365*, 757–763.
- Califano, F., C. Chiuderi, and G. Einaudi (1992), Nonresonant resistive dissipation of compressible magnetohydrodynamic waves, *Astrophys. J.*, *390*, 560–566.
- Carbone, V., and P. Veltri (1990), A shell model for anisotropic magnetohydrodynamic turbulence, *Geophys. Astrophys. Fluid Dyn.*, *52*(1–3), 153–181.
- Chen, C., S. Boldyrev, Q. Xia, and J. Perez (2013), Nature of subproton scale turbulence in the solar wind, *Phys. Rev. Lett.*, *110*(22), 225002.
- Davila, J. M. (1987), Heating of the solar corona by the resonant absorption of Alfvén waves, *Astrophys. J.*, *317*, 514–521.
- Décamp, N., and F. Malara (2006), Electron acceleration in turbulent coronal loops by kinetic Alfvén waves, in *SOHO-17. 10 Years of SOHO and Beyond*, vol. 617, p. 26., ESA Publ. Div., Noordwijk, Netherlands.
- Gary, S. P., and K. Nishimura (2004), Kinetic Alfvén waves: Linear theory and a particle-in-cell simulation, *J. Geophys. Res.*, *109*, A02109, doi:10.1029/2003JA010239.
- Ghosh, S., W. Matthaeus, D. Roberts, and M. Goldstein (1998), The evolution of slab fluctuations in the presence of pressure-balanced magnetic structures and velocity shears, *J. Geophys. Res.*, *103*(A10), 23,691–23,704.
- Goldstein, B. E., M. Neugebauer, L. D. Zhang, and S. P. Gary (2000), Observed constraint on proton-proton relative velocities in the solar wind, *Geophys. Res. Lett.*, *27*(1), 53–56.
- Goodrich, C., and A. Lazarus (1976), Suprathermal protons in the interplanetary solar wind, *J. Geophys. Res.*, *81*(16), 2750–2754.
- Greco, A., F. Valentini, S. Servidio, and W. Matthaeus (2012), Inhomogeneous kinetic effects related to intermittent magnetic discontinuities, *Phys. Rev. E*, *86*(6), 66405.
- Hellinger, P., and P. M. Trávníček (2011), Proton core-beam system in the expanding solar wind: Hybrid simulations, *J. Geophys. Res.*, *116*, A11101, doi:10.1029/2011JA016940.
- Hellinger, P., and P. M. Trávníček (2013), Protons and alpha particles in the expanding solar wind: Hybrid simulations, *J. Geophys. Res. Space Physics*, *118*, 5421–5430, doi:10.1002/jgra.50540.
- Heyvaerts, J., and E. Priest (1983), Coronal heating by phase-mixed shear Alfvén waves, *Astron. Astrophys.*, *117*, 220–234.
- Hollweg, J. V. (1987), Resonance absorption of magnetohydrodynamic surface waves physical discussion, *Astrophys. J.*, *312*, 880–885.
- Hollweg, J. V. (1999), Kinetic Alfvén wave revisited, *J. Geophys. Res.*, *104*(A7), 14,811–14,819.
- Howes, G., W. Dorland, S. Cowley, G. Hammett, E. Quataert, A. Schekochihin, and T. Tatsuno (2008a), Kinetic simulations of magnetized turbulence in astrophysical plasmas, *Phys. Rev. Lett.*, *100*(6), 65004.
- Howes, G. G., S. C. Cowley, W. Dorland, G. W. Hammett, E. Quataert, and A. A. Schekochihin (2008b), A model of turbulence in magnetized plasmas: Implications for the dissipation range in the solar wind, *J. Geophys. Res.*, *113*, A05103, doi:10.1029/2007JA012665.
- Kaghashvili, E. K. (1999), On the acceleration of the solar wind: Role of the inhomogeneous flow, *Astrophys. J.*, *512*(2), 969–974.
- Kappraff, J., and J. Tataronis (1977), Resistive effects on Alfvén wave heating, *J. Plasma Phys.*, *18*(02), 209–226.
- Kiyani, K. H., S. C. Chapman, F. Sahraoui, B. Hnat, O. Fauvarque, and Y. V. Khotyaintsev (2013), Enhanced magnetic compressibility and isotropic scale invariance at sub-ion larmor scales in solar wind turbulence, *Astrophys. J.*, *763*(1), 10, doi:10.1088/0004-637X/763/1/10.
- Landi, S., M. Velli, and G. Einaudi (2005), Alfvén waves and shock wave formation at an x-point magnetic field configuration, *The Astrophys. J.*, *624*(1), 392–401.
- Lee, M., and B. Roberts (1986), On the behavior of hydromagnetic surface waves, *Astrophys. J.*, *301*, 430–439.
- Lysak, R. L., and Y. Song (2011), Development of parallel electric fields at the plasma sheet boundary layer, *J. Geophys. Res.*, *116*, A00K14, doi:10.1029/2010JA016424.
- Malara, F., P. Veltri, C. Chiuderi, and G. Einaudi (1992), Incompressible disturbances in nonuniform media-formation of small scales, *Astrophys. J.*, *396*, 297–310.
- Malara, F., L. Primavera, and P. Veltri (1996), Formation of small scales via Alfvén wave propagation in compressible nonuniform media, *Astrophys. J.*, *459*, 347, doi:10.1086/176898.
- Malara, F., P. Petkaki, and P. Veltri (2000), Dissipation of Alfvén waves in force-free magnetic fields: Competition between phase mixing and three-dimensional effects, *Astrophys. J.*, *533*(1), 523–534.
- Malara, F., M. De Franceschis, and P. Veltri (2003), Alfvén wave propagation and dissipation in a 3D-structured compressible plasma, *Astron. Astrophys.*, *412*(2), 529–539.
- Malara, F., M. De Franceschis, and P. Veltri (2005), Dissipation of Alfvén waves in complex 3D coronal force-free structures, *Astron. Astrophys.*, *443*(3), 1033–1046.
- Malara, F., P. Veltri, and M. De Franceschis (2007), Alfvén wave dissipation and topological properties of 3D coronal force-free magnetic fields, *Astron. Astrophys.*, *467*(3), 1275–1284.
- Marsch, E. (2006), Kinetic physics of the solar corona and solar wind, *Living Rev. Sol. Phys.*, *3*(1), 1–100.
- Marsch, E., K.-H. Mühlhäuser, R. Schwenn, H. Rosenbauer, W. Pilipp, and F. Neubauer (1982), Solar wind protons: Three-dimensional velocity distributions and derived plasma parameters measured between 0.3 and 1 AU, *J. Geophys. Res.*, *87*(A1), 52–72.
- Matteini, L., S. Landi, M. Velli, and P. Hellinger (2010), Kinetics of parametric instabilities of Alfvén waves: Evolution of ion distribution functions, *J. Geophys. Res.*, *115*, A09106, doi:10.1029/2009JA014987.
- Matthaeus, W., M. Goldstein, and J. King (1986), An interplanetary magnetic field ensemble at 1 AU, *J. Geophys. Res.*, *91*(A1), 59–69.
- Matthaeus, W. H., M. L. Goldstein, and D. A. Roberts (1990), Evidence for the presence of quasi-two-dimensional nearly incompressible fluctuations in the solar wind, *J. Geophys. Res.*, *95*(20), 673–20.
- McLaughlin, J., A. Hood, and I. De Moortel (2011), Review article: MHD wave propagation near coronal null points of magnetic fields, *Space Sci. Rev.*, *158*(2–4), 205–236.
- Mok, Y., and G. Einaudi (1985), Resistive decay of Alfvén waves in a non-uniform plasma, *J. Plasma Phys.*, *33*(02), 199–208.
- Nakariakov, V., B. Roberts, and K. Murawski (1997), Alfvén wave phase mixing as a source of fast magnetosonic waves, *Sol. Phys.*, *175*(1), 93–105.
- Nakariakov, V., B. Roberts, and K. Murawski (1998), Nonlinear coupling of MHD waves in inhomogeneous steady flows, *Astron. Astrophys.*, *332*, 795–804.
- Nariyuki, Y., T. Hada, and K. Tsubouchi (2014a), Collisionless damping of circularly polarized nonlinear Alfvén waves in solar wind plasmas with and without beam protons, *Astrophys. J.*, *793*(2), 138.
- Nariyuki, Y., T. Umeda, T. Suzuki, and T. Hada (2014b), Ion acceleration by parallel propagating nonlinear Alfvén wave packets in a radially expanding plasma, *Nonlinear Process. Geophys.*, *21*(1), 339–346.
- Ofman, L., and M. Aschwanden (2002), Damping time scaling of coronal loop oscillations deduced from transition region and coronal explorer observations, *Astrophys. J. Lett.*, *576*(2), L153.

- Oughton, S., E. R. Priest, and W. H. Matthaeus (1994), The influence of a mean magnetic field on three-dimensional magnetohydrodynamic turbulence, *J. Fluid Mech.*, **280**, 95–117.
- Parashar, T. N., B. J. Vasquez, and S. A. Markovskii (2014), The role of electron equation of state in heating partition of protons in a collisionless plasma, *Phys. Plasmas*, **21**(2), 22301.
- Perrone, D., et al. (2014), Nonclassical transport and particle-field coupling: From laboratory plasmas to the solar wind, in *Microphysics of Cosmic Plasmas*, pp. 157–194, Springer, Netherlands.
- Petkaki, P., F. Malara, and P. Veltri (1998), Topological formation of small scales in magnetohydrodynamics: A fast dissipation mechanism, *Astrophys. J.*, **500**(1), 483.
- Podesta, J. J., and J. M. TenBarge (2012), Scale dependence of the variance anisotropy near the proton gyroradius scale: Additional evidence for kinetic Alfvén waves in the solar wind at 1 AU, *J. Geophys. Res.*, **117**, A10106, doi:10.1029/2012JA017724.
- Pucci, F., M. Onofri, and F. Malara (2014), Evolution of magnetohydrodynamic waves in low layers of a coronal hole, *Astrophys. J.*, **796**(1), 43.
- Ruderman, M. S., V. M. Nakariakov, and B. Roberts (1998), Alfvén wave phase mixing in two-dimensional open magnetic configurations, *Astron. Astrophys.*, **338**, 1118–1124.
- Sahraoui, F., M. Goldstein, P. Robert, and Y. V. Khotyaintsev (2009), Evidence of a cascade and dissipation of solar-wind turbulence at the electron gyroscale, *Phys. Rev. Lett.*, **102**(23), 231102.
- Sahraoui, F., G. Belmont, and M. Goldstein (2012), New insight into short-wavelength solar wind fluctuations from Vlasov theory, *Astrophys. J.*, **748**(2), 100.
- Salem, C., G. Howes, D. Sundkvist, S. Bale, C. Chaston, C. Chen, and F. Mozer (2012), Identification of kinetic Alfvén wave turbulence in the solar wind, *Astrophys. J. Lett.*, **745**(1), L9.
- Schekochihin, A., S. Cowley, W. Dorland, G. Hammett, G. Howes, E. Quataert, and T. Tatsuno (2009), Astrophysical gyrokinetics: Kinetic and fluid turbulent cascades in magnetized weakly collisional plasmas, *Astrophys. J. Suppl. Ser.*, **182**(1), 310–377.
- Servidio, S., F. Valentini, F. Califano, and P. Veltri (2012), Local kinetic effects in two-dimensional plasma turbulence, *Phys. Rev. Lett.*, **108**(4), 45001.
- Servidio, S., F. Valentini, D. Perrone, A. Greco, F. Califano, W. Matthaeus, and P. Veltri (2015), A kinetic model of plasma turbulence, *J. Plasma Phys.*, **81**, 1–35.
- Shebalin, J. V., W. H. Matthaeus, and D. Montgomery (1983), Anisotropy in MHD turbulence due to a mean magnetic field, *J. Plasma Phys.*, **29**(03), 525–547.
- Similon, P. L., and R. Sudan (1989), Energy dissipation of Alfvén wave packets deformed by irregular magnetic fields in solar-coronal arches, *Astrophys. J.*, **336**, 442–453.
- Steinolfson, R. (1985), Resistive wave dissipation on magnetic inhomogeneities normal modes and phase mixing, *Astrophys. J.*, **295**, 213–219.
- TenBarge, J., and G. Howes (2012), Evidence of critical balance in kinetic Alfvén wave turbulence simulations, *Phys. Plasmas*, **19**(5), 55901.
- Tomczyk, S., and S. W. McIntosh (2009), Time-distance seismology of the solar corona with coMP, *Astrophys. J.*, **697**(2), 1384–1391.
- Tomczyk, S., S. McIntosh, S. Keil, P. Judge, T. Schad, D. Seeley, and J. Edmondson (2007), Alfvén waves in the solar corona, *Science*, **317**(5842), 1192–1196.
- Tsiklauri, D. (2011), Particle acceleration by circularly and elliptically polarised dispersive Alfvén waves in a transversely inhomogeneous plasma in the inertial and kinetic regimes, *Phys. Plasmas*, **18**(9), 92903.
- Tsiklauri, D. (2012), Three dimensional particle-in-cell simulation of particle acceleration by circularly polarised inertial Alfvén waves in a transversely inhomogeneous plasma, *Phys. Plasmas*, **19**(8), 82903.
- Tsiklauri, D., and V. M. Nakariakov (2002), A three dimensional magnetohydrodynamic pulse in a transversely inhomogeneous medium, *Astron. Astrophys.*, **393**(1), 321–329.
- Tsiklauri, D., V. M. Nakariakov, and G. Rowlands (2003), Phase mixing of a three dimensional magnetohydrodynamic pulse, *Astron. Astrophys.*, **400**(3), 1051–1055.
- Tsiklauri, D., J.-I. Sakai, and S. Saito (2005), Particle-in-cell simulations of circularly polarised Alfvén wave phase mixing: A new mechanism for electron acceleration in collisionless plasmas, *Astron. Astrophys.*, **435**(3), 1105–1113.
- Tu, C.-Y., E. Marsch, and Z.-R. Qin (2004), Dependence of the proton beam drift velocity on the proton core plasma beta in the solar wind, *J. Geophys. Res.*, **109**, A05101, doi:10.1029/2004JA010391.
- Valentini, F., P. Trávníček, F. Califano, P. Hellinger, and A. Mangeney (2007), A hybrid-Vlasov model based on the current advance method for the simulation of collisionless magnetized plasma, *J. Comput. Phys.*, **225**(1), 753–770.
- Valentini, F., P. Veltri, F. Califano, and A. Mangeney (2008), Cross-scale effects in solar-wind turbulence, *Phys. Rev. Lett.*, **101**(2), 25006.
- Valentini, F., D. Perrone, and P. Veltri (2011a), Short-wavelength electrostatic fluctuations in the solar wind, *Astrophys. J.*, **739**(1), 54.
- Valentini, F., F. Califano, D. Perrone, F. Pegoraro, and P. Veltri (2011b), New ion-wave path in the energy cascade, *Phys. Rev. Lett.*, **106**(16), 165002.
- Valentini, F., S. Servidio, D. Perrone, F. Califano, W. Matthaeus, and P. Veltri (2014), Hybrid Vlasov-Maxwell simulations of two-dimensional turbulence in plasmas, *Phys. Plasmas*, **21**(8), 82307.
- Vasconez, C., F. Valentini, E. Camporeale, and P. Veltri (2014), Vlasov simulations of kinetic Alfvén waves at proton kinetic scales, *Phys. Plasmas*, **21**(11), 112107.
- Vasconez, C., F. Pucci, F. Valentini, S. Servidio, W. Matthaeus, and F. Malara (2015), Kinetic Alfvén wave generation by large-scale phase mixing, *Astrophys. J.*, **815**(1), 7.
- Voitenko, Y., and M. Goossens (2004), Cross-field heating of coronal ions by low-frequency kinetic Alfvén waves, *Astrophys. J. Lett.*, **605**(2), L149.
- Wu, D., and L. Chen (2013), Excitation of kinetic Alfvén waves by density striation in magneto-plasmas, *Astrophys. J.*, **771**(1), 3.